Check for updates

Advanced Science

ADVANCED SCIENCE Open Access

www.advancedscience.com

RESEARCH ARTICLE OPEN ACCESS

Machine-Learning-Driven Inverse Design of NURBS-Parameterized Auxetic Piezoelectric Energy Harvesters for Self-Powered Wireless Sensing

Shitong Fang[1,2] | Hongao Xue[1,2] | Keyu Chen[3] | Haobin Lin[1,2] | Miao Chen[4] | Liangdong Wei[4] | Qingyang Xu[5] | Qiang Gao[6] | Zhihui Lai[1,2] | Mingjing Cai[4] | Xiaoting Yuan[7] | Shuxiang Dong[8] | Liuchao Jin[3] | Wei-Hsin Liao[3,9]

[1]National Key Laboratory of Green and Long-Life Road Engineering in Extreme Environment (Shenzhen), Shenzhen University, Shenzhen, People's Republic of China | [2]College of Mechatronics and Control Engineering, Shenzhen University, Shenzhen, People's Republic of China | [3]Department of Mechanical and Automation Engineering, The Chinese University of Hong Kong, Hong Kong, People's Republic of China | [4]Guangzhou Institute of Technology and School of Mechano-Electronic Engineering, Xidian University, Guangzhou, People's Republic of China | [5]School of Mechatronic Engineering and Automation, Shanghai University, Shanghai, People's Republic of China | [6]School of Mechanical Engineering, Southeast University, Nanjing, People's Republic of China | [7]School of Advanced Manufacturing and Robotics, Peking University, Beijing, People's Republic of China | [8]School of Materials Science and Engineering, Peking University, Beijing, People's Republic of China | [9]Institute of Intelligent Design and Manufacturing, The Chinese University of Hong Kong, Hong Kong, People's Republic of China

Correspondence: Liuchao Jin (liuchao.jin@link.cuhk.edu.hk) | Wei-Hsin Liao (whliao@cuhk.edu.hk)

Received: 22 July 2026 | **Revised:** 23 September 2026 | **Accepted:** 28 October 2026

Keywords: auxetic metamaterials | inverse design | low-frequency vibration | machine learning | NURBS parameterization | piezoelectric energy harvesting | self-powered sensing

ABSTRACT

Low-frequency vibration energy is abundant in infrastructure, transportation, and industrial equipment, but piezoelectric harvesters face a power–stress-concentration trade-off: the large strain required for high output can intensify localized peak stress. In this paper, we develop a machine-learning-assisted inverse-design framework for NURBS-parameterized auxetic piezoelectric energy harvesters. NURBS control variables define a compact and continuous design space for curved re-entrant lattices, expanding deformation and load-transfer pathways beyond straight-wall geometries. A finite-element dataset generated by Latin hypercube sampling trains a neural-network surrogate to predict maximum average output power and peak von Mises stress from geometric parameters. Coupling this surrogate with NSGA-II enables co-optimization of electrical output and stress concentration. The optimized geometry increases effective biaxial stress/strain in the piezoelectric layer while redistributing localized stress. Under 0.5 g excitation at resonance, the optimized harvester delivers 7.56 mW maximum average output power and a normalized power density of 2.84×10^{-3} mW/(mm^3 · g^2 · Hz). Integrated with a self-powered LoRa sensing node, the device transmits temperature data over 150 m. This work offers a surrogate-assisted route to high-power, stress-aware energy harvesters and energy-autonomous IoT sensing.

1 | Introduction

Low-frequency ambient vibrations are widely distributed in industrial machinery, transportation systems, and civil infrastructure, providing a potentially sustainable energy source for powering wireless sensors, wearable electronics, and Internet-of-Things (IoT) devices [1–7]. Typical examples include railway tunnels, CNC machining equipment, and bridge structures. Har-

This is an open access article under the terms of the Creative Commons Attribution License, which permits use, distribution and reproduction in any medium, provided the original work is properly cited.
© 2026 The Author(s). *Advanced Science* published by Wiley-VCH GmbH

vesting such ubiquitous vibration energy is particularly attractive for enabling long-term autonomous operation of distributed sensing systems and reducing dependence on batteries [8]. However, despite substantial advances in piezoelectric energy harvesting technologies, efficient utilization of low-frequency vibrations remains a persistent challenge. Conventional piezoelectric cantilever harvesters generally exhibit limited power density under low-frequency excitation conditions, restricting their practical deployment in self-powered sensing and wireless monitoring applications [9, 10]. Consequently, enhancing the mechanical response of piezoelectric structures through geometric design has emerged as an important strategy for improving vibration energy harvesting performance [11–14]. In this work, low-frequency vibrations mainly refer to the sub-50 Hz regime relevant to infrastructure and machinery monitoring.

Among various geometric design approaches, auxetic structures with negative Poisson's ratio characteristics have attracted significant attention owing to their unique deformation mechanisms. Previous studies have demonstrated that integrating auxetic architectures into piezoelectric energy harvesters can substantially enhance electrical output under low-frequency excitations [15–24]. Such performance enhancement primarily originates from two mechanisms. First, auxetic structures generate biaxial strain amplification, which increases the effective strain experienced by piezoelectric materials. Second, their reduced equivalent stiffness facilitates stronger dynamic responses in the low-frequency regime. Nevertheless, these advantages introduce an inherent trade-off. Increasing deformation and strain levels can intensify localized stress concentration within the structure [11]. As a result, the design of auxetic piezoelectric energy harvesters is fundamentally governed by a conflict between maximizing electrical power generation and minimizing peak stress concentration. Resolving this power–stress-concentration trade-off is essential for developing stress-aware auxetic energy harvesting systems.

Identifying optimal auxetic geometries is considerably more difficult than optimizing conventional piezoelectric structures because of the highly nonlinear relationship between geometry, deformation behavior, stress distribution, and electromechanical performance. Existing design approaches can be broadly categorized into three classes. The first relies on parameter scanning and empirical design methodologies [25–30], which often explore only a limited portion of the design space. The second employs forward finite-element-based optimization, where repeated numerical simulations are performed to iteratively improve structural performance [31–41]. Although capable of identifying improved configurations, these methods become computationally prohibitive when the geometric design space is large and highly nonlinear. More recently, machine-learning-assisted optimization strategies have shown promise in accelerating design exploration and reducing computational cost [42–52]. However, two design challenges remain particularly relevant for continuously varying auxetic morphologies: (i) representing detailed curvilinear boundaries using a compact and physically interpretable set of design variables, and (ii) integrating such a geometric representation with an efficient surrogate-assisted multi-objective search that links structural geometry to competing performance objectives. Consequently, achieving simultaneous optimization of electrical output and peak stress concentration remains an open challenge [53].

For predefined straight re-entrant auxetic cells, commonly used geometric descriptors include ligament lengths, re-entrant angle, unit-cell dimensions, wall thickness, ligament width, and selected junction coordinates [54]. These parameters provide an efficient and physically intuitive description when the topology and geometric primitives are fixed. When the detailed curvilinear boundary itself becomes a design variable, however, such global descriptors provide only indirect control over local boundary shape. Dense boundary-point [55, 56], mesh-node [57], pixel [58], or voxel [59–62] descriptions can provide greater shape freedom, but the number of independent design variables generally increases with geometric resolution. These considerations make geometric representation a key interface between structural shape generation and data-driven optimization. For the present problem, an appropriate representation should provide direct and continuous control over curved ligament profiles using a compact, fixed set of design variables, while remaining independent of the spatial discretization subsequently used in finite-element analysis.

As illustrated in Figure 1c, Non-Uniform Rational B-Splines (NURBS) provide such a representation because selected control points can continuously regulate the curved auxetic geometry through a compact and physically interpretable set of variables while preserving geometric continuity [63–67]. Accordingly, Figure 1a,b compares the established straight re-entrant auxetic architecture with its NURBS-parameterized counterpart. The former serves as the reference, whereas the latter introduces continuous control of the curved ligament profiles and defines the geometric design space explored in the subsequent inverse-design procedure. When integrated with data-driven surrogate models, such a representation provides a pathway for transforming the conventional paradigm of computationally intensive forward exploration into an efficient inverse-design framework capable of navigating large design spaces [68, 69].

In this paper, we present a machine-learning-assisted, surrogate-based inverse-design framework for auxetic piezoelectric energy harvesters based on NURBS geometric parameterization. The framework combines compact and continuous geometric representation, data-driven surrogate modeling, and multi-objective evolutionary optimization within a unified design workflow (Figure 1d). Specifically, auxetic geometries are parameterized using a NURBS-based description that provides continuous geometric flexibility through a compact set of control-point variables within a prescribed bounded design space. A structured geometry–performance dataset is subsequently constructed through optimal Latin hypercube sampling and finite-element simulations, from which a neural-network surrogate model is trained to establish the nonlinear relationship between geometric morphology and electromechanical performance. By coupling the surrogate model with the NSGA-II algorithm, the framework enables simultaneous optimization of electrical power output and peak stress, thereby addressing the power–stress-concentration trade-off between energy harvesting efficiency and stress-aware structural design. The optimized design is further integrated into a self-powered long-range (LoRa) wireless sensing platform comprising rectification and energy storage,

21983844, 0, Downloaded from https://advanced.onlinelibrary.wiley.com/doi/10.1002/advs.78735 by Liuchao Jin , Wiley Online Library on [18/11/2026]. See the Terms and Conditions (https://onlinelibrary.wiley.com/terms-and-conditions) on Wiley Online Library for rules of use; OA articles are governed by the applicable Creative Commons License

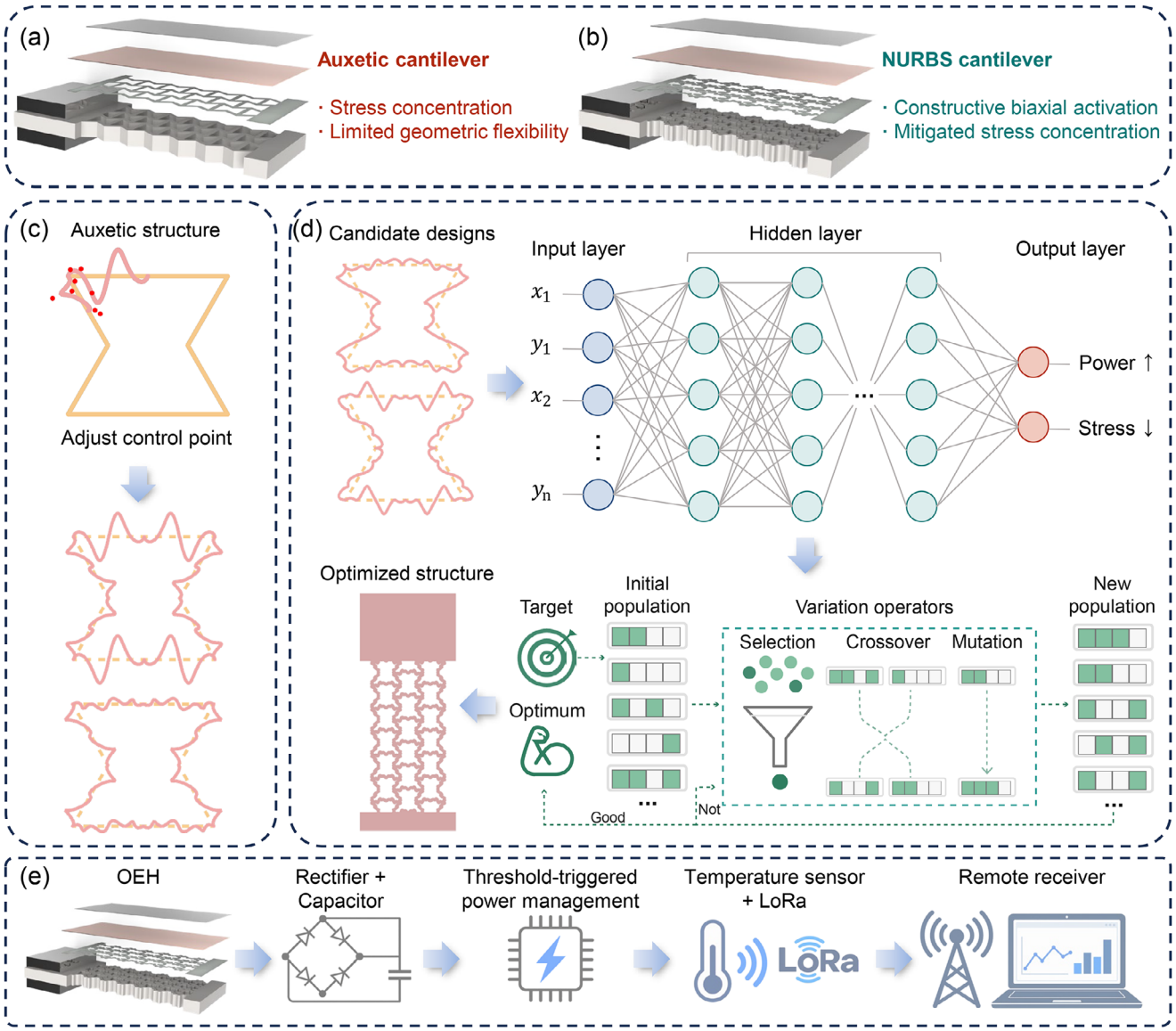


FIGURE 1 | Conceptual overview of the NURBS-enabled, machine-learning-assisted inverse-design framework for auxetic piezoelectric energy harvesting and self-powered wireless sensing. (a) Straight re-entrant auxetic piezoelectric cantilever architecture. (b) NURBS-parameterized re-entrant auxetic piezoelectric cantilever architecture. (c) NURBS parameterization of the auxetic unit cell, where selected control points are adjusted to generate continuously varied candidate geometries. (d) Surrogate-assisted multi-objective inverse-design workflow. (e) System-level demonstration of the optimized energy harvester (OEH) for self-powered wireless sensing.

threshold-triggered power management, temperature sensing, wireless transmission, and remote data reception (Figure 1e). Under a base excitation of 0.5 g (approximately 4.9 m s^{-2}), the resulting harvester achieves a maximum average output power of 7.56 mW and a normalized power density of 2.84×10^{-3} mW/($mm^3 \cdot g^2 \cdot Hz$), while enabling non-line-of-sight wireless sensing over a transmission distance of 150 m. Together, these results position NURBS-enabled inverse design as a scalable strategy for balancing output power and stress concentration in self-powered sensing systems. The methodological contribution of the present study lies in integrating a continuous NURBS-based geometric representation with a stress-aware surrogate-assisted multi-objective inverse-design workflow for auxetic piezoelectric energy harvesters, followed by finite-element, experimental, and system-level validation. In this framework, NURBS defines the optimization-compatible geometry space, the neural network provides rapid forward performance evaluation, NSGA-II explores the power–stress Pareto trade-off, and the LoRa platform serves as application-level validation of the selected optimized harvester.

2 | Results and Discussion

2.1 | Structural Design and Electromechanical Modeling

This section describes the NURBS-parameterized auxetic cantilever energy harvester and the geometric modeling workflow shown in Figure 2. Conventional cantilever piezoelectric energy harvesters mainly generate charge from bending-induced strain concentrated near the clamped root. In an auxetic substrate, the

21983844, 0, Downloaded from https://advanced.onlinelibrary.wiley.com/doi/10.1002/advs.70735 by Liuchao Jin , Wiley Online Library on [18/11/2026]. See the Terms and Conditions (https://onlinelibrary.wiley.com/terms-and-conditions) on Wiley Online Library for rules of use; OA articles are governed by the applicable Creative Commons License

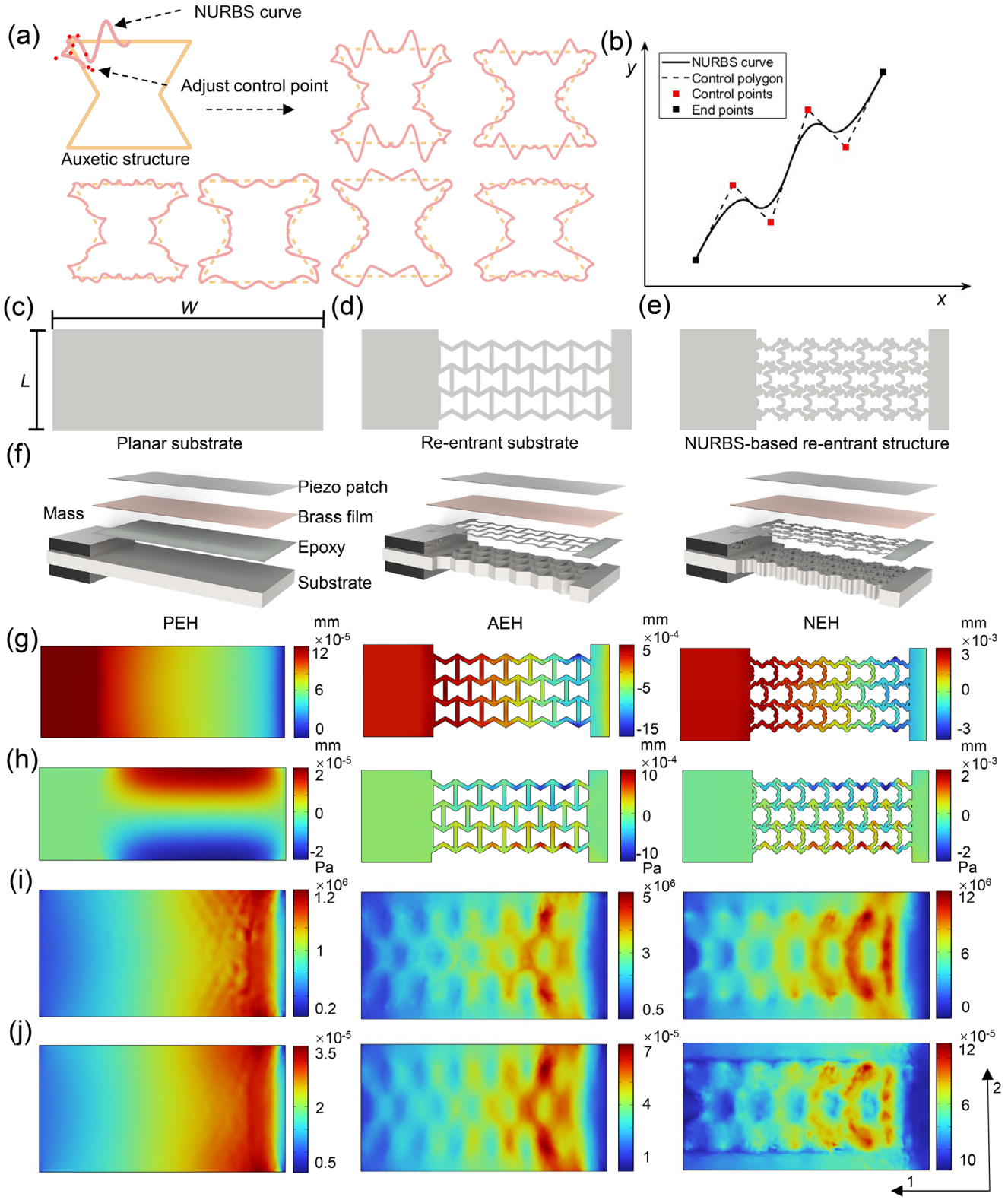


FIGURE 2 | Geometric modeling and finite-element simulation results of the piezoelectric energy harvesters. (a) NURBS control points schematic. (b) NURBS curve representation. (c–e) Planar, straight re-entrant, and NURBS-based re-entrant substrates. (f) Layered device architectures of the PEH, AEH, and NEH. (g) Longitudinal displacement contours under identical boundary and loading conditions. (h) Transverse displacement contours under identical boundary and loading conditions. (i) Stress distribution in the piezoelectric layer, illustrating the extended high-stress region enabled by auxetic designs. (j) Strain distribution in the piezoelectric layer, highlighting the improved average strain level and distribution uniformity achieved by the NURBS-governed auxetic substrate.

21983844, 0, Downloaded from https://advanced.onlinelibrary.wiley.com/doi/10.1002/advs.78735 by Liuchao Jin , Wiley Online Library on [18/11/2026]. See the Terms and Conditions (https://onlinelibrary.wiley.com/terms-and-conditions) on Wiley Online Library for rules of use; OA articles are governed by the applicable Creative Commons License

in-plane deformation field can redistribute strain over a larger piezoelectric area and alter the electromechanical response. The design objective is therefore to use auxetic geometry to amplify useful piezoelectric strain while limiting stress concentration. Based on the constitutive equations of lead zirconate titanate (PZT), and under the following assumptions of sinusoidal steady-state excitation, compatible electrode/polarization configuration, and spatially averaged in-plane stress, the governing electromechanical relations are expressed as follows:

$$T_{ij} = c^{E}_{ijkl} S_{kl} - e_{kij} E_k \tag{1}$$

$$D_i = e_{ikl} S_{kl} + \varepsilon^{S}_{ik} E_k \tag{2}$$

where T_{ij} (Pa), S_{kl} (dimensionless), E_k (V m^{-1}), and D_i (C m^{-2}) denote the mechanical stress tensor, mechanical strain tensor, electric field vector, and electric displacement vector, respectively. The material constants c^{E}_{ijkl} (Pa), e_{kij} (C m^{-2}), and ε^{S}_{ik} (F m^{-1}) denote the elastic stiffness at constant electric field, piezoelectric stress constant, and dielectric permittivity at constant strain (clamped condition), respectively. Here, the superscripts E, S, and T indicate the quantities held constant in the corresponding material coefficients, namely electric field, strain, and stress, respectively. Owing to the auxetic architecture, the in-plane stress and strain fields in the piezoelectric layer are redistributed and amplified, which can increase electrical power density when the stress components constructively contribute to charge generation. For the present PZT-5H patch polarized along the thickness direction, the dominant electromechanical response is associated with the in-plane transverse piezoelectric coupling. According to the linear piezoelectric constitutive relation, the spatially averaged electric displacement in the polarization direction is $\bar{D}_3 = d_{31}\bar{\sigma}_{11} + d_{32}\bar{\sigma}_{22} + \varepsilon^{T}_{33}E_3$, where d_{31} and d_{32} (C N^{-1}) denote the transverse piezoelectric strain coefficients coupling the in-plane normal stresses σ_{11} and σ_{22}, respectively, to the electric displacement in the polarization direction. Under open-circuit conditions, the net free charge on the electrodes vanishes, and the through-thickness electric field is assumed to be approximately uniform. Thus, $\bar{D}_3 = 0, E_3 \approx -U_{oc}/t_p$. Since the two transverse piezoelectric coefficients adopted for the PZT-5H material are identical, the open-circuit voltage can be approximated as follows:

$$|U_{oc}| = \left| \frac{d_{31} t_p}{\varepsilon^{T}_{33}} (\bar{\sigma}_{11} + \bar{\sigma}_{22}) \right| \tag{3}$$

where t_p (m) is the piezoelectric-layer thickness, and ε^{T}_{33} (F m^{-1}) is the dielectric permittivity at constant stress in the thickness direction. It is related to the dimensionless relative permittivity ($\varepsilon^{T}_{r,33}$), which represents the dielectric permittivity in the thickness direction relative to the vacuum permittivity under constant-stress conditions, through $\varepsilon^{T}_{33} = \varepsilon_0 \varepsilon^{T}_{r,33}$, where ε_0 is the vacuum permittivity. U_{oc} (V) denotes the open-circuit peak voltage amplitude, while $\bar{\sigma}_{11}$ and $\bar{\sigma}_{22}$ (Pa) denote the spatially averaged longitudinal and transverse normal stresses in the piezoelectric layer, respectively. Equation (3) therefore indicates that the longitudinal and transverse average in-plane stresses jointly contribute to the open-circuit voltage, and their constructive contribution can enhance the electromechanical response of the auxetic configuration.

For harmonic excitation, the piezoelectric element is represented by the linear Thevenin equivalent of an open-circuit sinusoidal voltage source in series with a capacitive impedance. The corresponding circuit quantities are

$$Z_C = \frac{1}{j\omega C_p}, \qquad C_p = \frac{\varepsilon^{T}_{33} A_p}{t_p}, \qquad \omega = 2\pi f \tag{4}$$

where the source peak amplitude is the open-circuit voltage defined above. The magnitude of the capacitive reactance is

$$|X_C| = \frac{1}{2\pi f C_p} \tag{5}$$

For a purely resistive load, the load-voltage peak amplitude is

$$V_{L,\mathrm{peak}} = U_{oc} \frac{R_L}{\sqrt{R_L^2 + |X_C|^2}} \tag{6}$$

The corresponding loaded RMS voltage is

$$V_{L,\mathrm{RMS}} = \frac{V_{L,\mathrm{peak}}}{\sqrt{2}} \tag{7}$$

and the average load power is consequently

$$P(R_L) = \frac{V^2_{L,\mathrm{RMS}}}{R_L} = \frac{U^2_{oc}}{2} \frac{R_L}{R_L^2 + |X_C|^2} \tag{8}$$

where R_L is the external resistive load connected to the piezoelectric harvester. Maximizing this expression with respect to the resistive load gives the impedance-matching condition and hence the optimal load resistance

$$R_{\mathrm{opt}} = |X_C| = \frac{1}{2\pi f C_p} = \frac{t_p}{2\pi f \varepsilon^{T}_{33} A_p} \tag{9}$$

At the optimum load, the loaded peak and RMS voltages become

$$V_{L,\mathrm{peak}} = \frac{U_{oc}}{\sqrt{2}}, \qquad V_{L,\mathrm{RMS}} = \frac{U_{oc}}{2} \tag{10}$$

Substitution into the load-power expression gives

$$P_{\max} = \frac{V^2_{L,\mathrm{RMS}}}{R_{\mathrm{opt}}} = \frac{U^2_{oc}}{4R_{\mathrm{opt}}} = \frac{\pi f t_p A_p d^2_{31}}{2\varepsilon^{T}_{33}} (\bar{\sigma}_{11} + \bar{\sigma}_{22})^2. \tag{11}$$

Here, the symbols correspond respectively to the optimal resistive load, excitation frequency, piezoelectric capacitance, and electrode area: R_{opt} (Ω), f (Hz), C_p (F), A_p (m^2). Equation (11) therefore indicates that, within this simplified analytical model, the maximum output power is proportional to the square of the effective biaxial average-stress contribution. $P_{\max} \propto (\bar{\sigma}_{11} + \bar{\sigma}_{22})^2$. These analytical relations are primarily used to explain the electromechanical coupling mechanism and assume linear piezoelectric behavior, single-frequency steady-state excitation, continuous electrodes, dominant in-plane piezoelectric coupling, an approximately uniform through-thickness electric field, and a lumped capacitive piezoelectric model connected to a purely resistive load. Equation (9) therefore provides an approximate

21983844, 0, Downloaded from https://advanced.onlinelibrary.wiley.com/doi/10.1002/advs.79735 by Liuchao Jin , Wiley Online Library on [18/11/2026]. See the Terms and Conditions (https://onlinelibrary.wiley.com/terms-and-conditions) on Wiley Online Library for rules of use; OA articles are governed by the applicable Creative Commons License

impedance-matching resistance. In the experiments, the actual optimal load resistance was determined from the measured resistance-sweep results using $P = V_{\mathrm{RMS}}^2/R$. The expressions for open-circuit voltage and $P_{max} \propto (\bar{\sigma}_{11} + \bar{\sigma}_{22})^2$ indicate that, under the assumed electrode configuration, constructive contributions from the average longitudinal stress $\bar{\sigma}_{11}$ and transverse stress $\bar{\sigma}_{22}$ can increase the electrical output. In cantilever substrates with a positive effective Poisson's ratio, longitudinal bending strain is accompanied by transverse contraction or expansion that can reduce the net electromechanically active stress contribution. This partial cancellation can limit U_{oc} and P_{max} by reducing the effective biaxial stress term in the piezoelectric layer. Introducing a negative-Poisson's-ratio auxetic substrate mitigates this limitation by promoting in-plane deformation compatibility. Re-entrant rotation and cell-wall bending can produce transverse expansion that is *in-phase* with longitudinal tensile strain during bending. This response allows the transverse stress component to contribute constructively with the longitudinal stress. Within the simplified analytical formulation, this change increases the effective biaxial term $(\bar{\sigma}_{11} + \bar{\sigma}_{22})^2$. The resulting biaxial strain-amplified state is expected to increase both open-circuit voltage and maximum output power. Furthermore, auxetic structures are often associated with reduced stiffness and large deformation characteristics. Under identical external excitation, this compliance facilitates a higher curvature of the substrate, consequently augmenting the absolute peak magnitude of $\bar{\sigma}_{11}$.

Therefore, the re-entrant auxetic honeycomb substrate is designed to improve output power through biaxial strain amplification and a lower-frequency dynamic response relative to a conventional solid cantilever. Figure 2 summarizes the geometric modeling and finite-element analysis workflow of the auxetic energy harvester investigated in this study. Figure 2a illustrates the adjustment of selected NURBS control points to continuously modify the re-entrant auxetic unit-cell contour and generate candidate geometries. The re-entrant auxetic unit cell consists of two types of ligaments: horizontal ligaments and inclined ligaments. Four control points were placed along the central half of the horizontal ligament, while another four control points were placed along the central half of the inclined ligament. These control points were connected using NURBS curves to define the corresponding smooth ligament profiles. The remaining portions of the unit cell were then generated through axial and central symmetry operations, yielding a diverse set of NURBS-based re-entrant geometries with negative Poisson's ratios, as illustrated in Figure 2a. Figure 2b presents the corresponding NURBS curve representation, including the control polygon, control points, end points, and the resulting smooth curve. During candidate-geometry generation, the control-point ranges were imposed as explicit design-space restrictions (Table S1). The structural wall thickness was fixed at 1.1 mm primarily to place the characteristic frequency within the intended low-frequency range. This value was also compatible with the adopted 3D-printing process, but was not introduced as a separate minimum-thickness optimization constraint. Minimum curvature radius, automated self-intersection detection, automated connectivity checking, and printer resolution were not formulated as independent mathematical constraints. The final OEH geometry selected from the candidate designs was subsequently reconstructed in the finite-element model and fabricated for experimental evaluation.

TABLE 1 | Geometric parameters of the energy harvester.

Component	Parameter	Symbol	Value	Unit
Piezoelectric patch	Length	L_p	60	mm
	Width	W_p	31	mm
	Thickness	T_p	0.2	mm
Cantilever beam	Length	L_b	88	mm
	Width	W_b	33	mm
	Thickness	T_b	5	mm
Brass substrate	Length	L_c	66	mm
	Width	W_c	33	mm
	Thickness	T_c	0.2	mm
Proof mass	Length	L_m	20	mm
	Width	W_m	30	mm
	Thickness	T_m	5	mm
Epoxy layer	Thickness	T_e	0.1	mm

Figure 2c–e compares the planar substrate used in the conventional piezoelectric energy harvester (PEH), the straight re-entrant substrate used in the auxetic energy harvester (AEH), and the NURBS-based re-entrant substrate used in the NURBS-based energy harvester (NEH), respectively. The NURBS basis provides flexibility for representing complex curvilinear geometries, while the control-point coordinates and weights enable smooth geometry tuning with a compact set of design variables. Figure 2f compares the layered device architectures of the PEH, AEH, and NEH, including the proof mass, piezoelectric patch, brass film, epoxy layer, and elastic substrate.

2.2 | Finite Element Modeling

Finite element analysis (FEA) was used to resolve the coupled mechanical and electrical responses of the energy harvesters with complex substrate geometries. The model was established in COMSOL Multiphysics 6.3 using the Solid Mechanics, Electrostatics, and Electrical Circuit interfaces, with electromechanical coupling implemented through the piezoelectric multiphysics interface. To elucidate the advantages conferred by integrating a conventional straight hexagonal honeycomb structure (exhibiting negative Poisson's ratio) with Non-Uniform Rational B-Spline (NURBS) curves, numerical models are constructed for the straight re-entrant auxetic energy harvester (AEH), the NURBS-based auxetic energy harvester (NEH), and the conventional planar piezoelectric energy harvester (PEH). The three investigated configurations share identical overall dimensions. The piezoelectric buzzer element is bonded to the elastic substrate layer via an epoxy resin adhesive, with the substrate layer fabricated through additive manufacturing (3D printing). The geometric parameters and material properties of the energy harvesters are summarized in Tables 1 and 2, respectively.

The computational domains were discretized using a free tetrahedral mesh with region-specific mesh controls. The piezoelectric layer was meshed with a minimum element size of 0.2 mm, while the adhesive layer was refined using a minimum element

21983844, 0, Downloaded from https://advanced.onlinelibrary.wiley.com/doi/10.1002/advs.79735 by Liuchao Jin , Wiley Online Library on [18/11/2026]. See the Terms and Conditions (https://onlinelibrary.wiley.com/terms-and-conditions) on Wiley Online Library for rules of use; OA articles are governed by the applicable Creative Commons License

TABLE 2 | Material properties of the energy harvester.

Component	Parameter	Symbol	Value	Unit
Cantilever beam	Density	ρ_b	1200	kgm^{-3}
	Young's Modulus	E_b	2.3	GPa
	Poisson's Ratio	μ_b	0.36	—
PZT-5A patch	Density	ρ_p	7750	kgm^{-3}
	Compliance matrix	S_{11}	1.64×10^{-11}	Pa^{-1}
		S_{12}	-5.74×10^{-12}	Pa^{-1}
		S_{13}	-7.22×10^{-12}	Pa^{-1}
		S_{22}	1.64×10^{-11}	Pa^{-1}
		S_{23}	-7.22×10^{-12}	Pa^{-1}
		S_{33}	1.88×10^{-11}	Pa^{-1}
		S_{44}	4.75×10^{-11}	Pa^{-1}
		S_{55}	4.75×10^{-11}	Pa^{-1}
	Coupling matrix	d_{31}	-1.71×10^{-10}	CN^{-1}
		d_{32}	-1.71×10^{-10}	CN^{-1}
		d_{33}	3.74×10^{-10}	CN^{-1}
		d_{24}	5.84×10^{-10}	CN^{-1}
		d_{15}	5.84×10^{-10}	CN^{-1}
	Relative permittivity (constant stress)	$\varepsilon^T_{r,33}$	826	—
Brass substrate	Density	ρ_c	8960	kgm^{-3}
	Young's Modulus	E_c	120	GPa
	Poisson's Ratio	μ_c	0.35	—
Epoxy layer	Density	ρ_e	1100	kgm^{-3}
	Young's Modulus	E_e	0.03	GPa
	Poisson's Ratio	μ_e	0.35	—
Proof mass (Steel)	Density	ρ_m	7316	kgm^{-3}
	Young's Modulus	E_m	200	GPa
	Poisson's Ratio	μ_m	0.30	—

size of 0.1 mm to adequately resolve its thin geometry. For the auxetic substrate, a global mesh size of 3.44 mm was adopted, together with adaptive mesh refinement to provide finer elements in regions requiring increased spatial resolution, particularly around curved features and geometric transitions. The remaining mesh-control parameters included a curvature factor of 0.8 and a narrow-region resolution of 0.3. Mesh convergence was checked before the final calculations by progressively refining the mesh and confirming that the resonant frequency and electrical output response no longer changed appreciably. The clamped end of each harvester was fixed, while the remaining external surfaces were free. Base excitation was applied as an equivalent inertial body load in the Z direction. The piezoelectric electrodes were coupled to an external electrical circuit with variable load resistance, and Rayleigh damping was applied to the model. The analysis sequence consisted of an eigenfrequency study followed by frequency-domain analysis and load-resistance parameter sweeps. Linear-elastic material behavior was assumed, and geometric and material nonlinearities were not included.

Figure 2 presents the finite element simulation results for three piezoelectric cantilever beams with different substrate configurations under identical boundary and loading conditions, analyzed across four dimensions: longitudinal displacement, transverse displacement, stress distribution in the piezoelectric layer, and strain distribution. Here, longitudinal displacement refers to the displacement along direction 1 defined in Figure 2. From the comparison of longitudinal displacement contours (Figure 2g), the conventional solid-substrate cantilever beam exhibits a typical linear increasing deflection profile from the root to the free end, featuring a uniform displacement gradient but limited amplitude. In contrast, the cantilever beam with the straight internal-hexagon auxetic substrate produces a significantly larger longitudinal displacement amplitude at the free end, attributable to the cell-wall bending-dominated deformation mechanism and the overall structural stiffness softening effect. The NURBS-based substrate retains the large-deformation response while exhibiting a smoother longitudinal displacement distribution. Using the root-mean-square second-order difference of the normalized longitudinal displacement profile as a displacement-field roughness

21983844, 0, Downloaded from https://advanced.onlinelibrary.wiley.com/doi/10.1002/advs.79735 by Liuchao Jin , Wiley Online Library on [18/11/2026]. See the Terms and Conditions (https://onlinelibrary.wiley.com/terms-and-conditions) on Wiley Online Library for rules of use; OA articles are governed by the applicable Creative Commons License

index (defined in Section S4), the value decreases from 0.0135 for the straight re-entrant AEH to 0.0088 for the NURBS-based NEH, corresponding to a 34.8% reduction.

The differences in transverse displacement distribution (Figure 2h) show the extent to which the auxetic effect is activated. When the conventional cantilever beam undergoes positive bending, constrained by its positive Poisson's ratio, the piezoelectric layer region exhibits distinct transverse contraction (negative displacement), which directly results in the negative contribution of the σ_{22} term in the aforementioned theoretical formulation. The straight internal-hexagon substrate displays the opposite behavior: in the longitudinally stretched region, the transverse displacement manifests as an expansion of the same sign, verifying the successful activation of the effective negative Poisson's ratio of the structure. The NURBS-governed substrate further improves the uniformity of transverse expansion. The results of stress distribution (Figure 2i) and strain distribution (Figure 2j) in the piezoelectric layer further quantify the discrepancy in energy harvesting performance. For the conventional cantilever beam, the stress in the piezoelectric layer is highly concentrated in the root region and exhibits a pronounced gradient decay—large in the center and small toward the edge—along the width direction, such that the volume fraction of the high-stress region effectively contributing to electromechanical conversion is limited. Through the bending-hinge effect of the cell walls, the straight internal-hexagon substrate forms a more extensive stress plateau region when transferring the external load to the piezoelectric layer, with the high-stress region extending significantly from the root toward the free end. As shown by the strain distribution in Figure 2j, the NURBS configuration achieves the highest average strain level within the piezoelectric layer and distributes the active strain over a broader region.

2.3 | Machine Learning Enabled Forward Prediction

Auxetic piezoelectric energy harvesters exhibit strong geometry-dependent electromechanical behavior, where slight variations in structural morphology can lead to significant changes in deformation characteristics, stress distribution, and electrical output performance. However, owing to the high-dimensional continuous design space introduced by geometric parameterization and the inherently nonlinear coupling between structural geometry and multiphysics responses, direct exploration of the design space through exhaustive finite-element simulations becomes computationally expensive and practically infeasible. Particularly for multi-objective optimization problems involving conflicting performance metrics, thousands of design evaluations are typically required, resulting in prohibitively high computational costs. Therefore, the development of an accurate and computationally efficient surrogate model is essential for accelerating the design process and enabling inverse optimization of auxetic energy harvesters [70–72]. In this work, inverse design refers to a surrogate-assisted multi-objective search in which NURBS-defined geometric variables are searched from the desired performance directions of maximizing power and minimizing peak stress; no fixed scalar target values for power or stress are prescribed in advance.

To address this challenge, a machine-learning-assisted inverse design framework is established, as illustrated in Figure 3a. The proposed framework integrates three key components into a unified workflow: NURBS-based geometric parameterization, neural-network surrogate modeling, and NSGA-II-based multi-objective optimization. Two independent Latin-hypercube sampling (LHS) sets were generated within the same prescribed bounded 16-dimensional NURBS control-point design space. The training candidate pool initially contained 1900 geometries, whereas a separate LHS set of 100 geometries was generated for validation. After geometric screening and finite-element preprocessing were performed independently for the two candidate pools, 187 training candidates and 10 validation candidates were excluded, leaving 1713 valid training samples and 90 valid validation samples, respectively. Thus, 2000 candidate geometries were generated in total, of which 1803 yielded valid finite-element samples and 197 were excluded during preprocessing. The overall retention and exclusion rates were 90.15% and 9.85%, respectively. Among the 1803 valid samples, the training and validation datasets accounted for 95.01% and 4.99%, respectively, corresponding to an approximate training-to-validation sample-count ratio of 19:1. Because the validation geometries were generated through a separate LHS procedure, they were not members of the training candidate pool. The validation samples were not used for gradient-based network-parameter fitting; instead, they were used to monitor validation performance and support the selection of the network architecture and training hyperparameters. No third independent test dataset was used in the present study. Latin-hypercube sampling stratifies each individual design-variable range, while the two-dimensional coordinate-pair projections in Figure S1 are used to visualize the sampled marginal and pairwise distributions across the prescribed coordinate bounds.

Specifically, the auxetic topology is parameterized using Non-Uniform Rational B-Splines (NURBS), whereby the structural geometry is represented through the coordinates of selected control points. Compared with dense boundary-point, mesh-node, pixel, or voxel descriptions of curved boundaries, the adopted NURBS representation provides a compact and continuous parameterization without implying a universally lower dimensionality than all simple analytical geometries. The surrogate-model inputs are the 16 physical control-point coordinates in millimeters. Before neural-network training, each input feature and both output quantities are standardized using the mean and standard deviation of the training set through StandardScaler; the same fitted scalers are then applied to the validation data.

A feedforward artificial neural network (ANN) is employed to establish the nonlinear mapping between the geometric parameters and the corresponding device performance. As shown in Figure 3a, the feedforward network contains 16 input features, four fully connected hidden layers, and two output neurons. The first hidden layer contains 398 neurons, and the width of each subsequent hidden layer is progressively reduced to approximately one-half of that of the preceding layer. A ReLU activation and batch normalization are applied after each hidden layer, while Dropout with a rate of 0.3 is applied only after the third hidden layer. Training uses the Adam optimizer with a learning rate of 2×10^{-3}, a batch size of 64, 1000 epochs, and mean-squared error (MSE) evaluated in the standardized

21983844, 0, Downloaded from https://advanced.onlinelibrary.wiley.com/doi/10.1002/advs.78735 by Liuchao Jin , Wiley Online Library on [18/11/2026]. See the Terms and Conditions (https://onlinelibrary.wiley.com/terms-and-conditions) on Wiley Online Library for rules of use; OA articles are governed by the applicable Creative Commons License

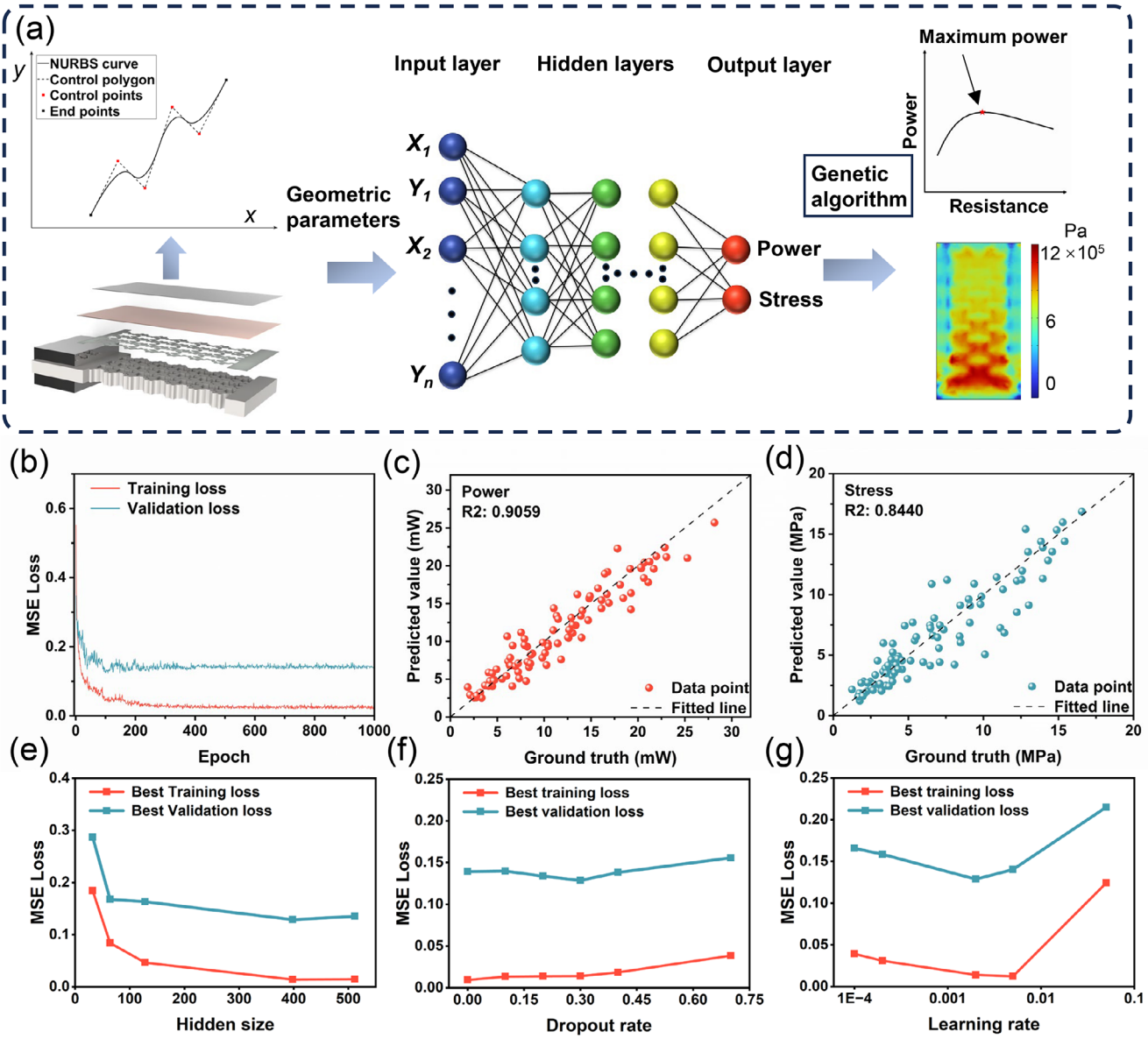


FIGURE 3 | Integrated machine-learning-assisted inverse design framework for auxetic piezoelectric energy harvesters. (a) Overall optimization framework. (b) Training and validation loss histories. (c) Power prediction performance. (d) Stress prediction performance. (e–g) Hyperparameter sensitivity analyses showing the effects of hidden-layer size, dropout rate, and learning rate on the training and validation losses, respectively.

output space. The linear-layer parameters use the default PyTorch initialization. The two output neurons use linear activations because both target quantities are continuous regression variables. The network simultaneously predicts two key performance indicators: maximum average output power and peak von Mises stress (hereafter, peak stress). The former characterizes the energy harvesting capability of the device, whereas the latter serves as a stress-concentration indicator relevant to stress-aware structural design.

By learning from the multiphysics finite-element simulation dataset, the surrogate model captures the dominant geometry–performance relationships and replaces repeated finite-element evaluations during the evolutionary search. Maximizing electrical output and minimizing peak stress are treated as competing objectives. Different geometries within the design space can redistribute deformation and produce different levels of local peak von Mises stress; in this work, the maximum von Mises stress is used as a quantitative comparative indicator of local stress concentration rather than as an experimentally calibrated failure threshold or fatigue-life criterion. Thus, the optimization seeks high electrical output while suppressing localized high-stress regions within the same material and loading framework. To simultaneously address these competing requirements, the trained neural-network surrogate model is coupled with the Non-dominated Sorting Genetic Algorithm II (NSGA-II), forming a multi-objective inverse design framework capable of efficiently searching for Pareto-optimal solutions.

The predictive performance of the neural-network surrogate model is assessed using the training and separately generated validation datasets. Figure 3b presents the evolution of the training and validation losses. Both curves decrease rapidly during the initial training stage and approach stable values without

21983844, 0, Downloaded from https://advanced.onlinelibrary.wiley.com/doi/10.1002/advs.78735 by Liuchao Jin , Wiley Online Library on [18/11/2026]. See the Terms and Conditions (https://onlinelibrary.wiley.com/terms-and-conditions) on Wiley Online Library for rules of use; OA articles are governed by the applicable Creative Commons License

a pronounced separation for this specific training/validation configuration. Figure 3c,d compares surrogate predictions with finite-element results for the validation samples. The coefficients of determination are $R^2 = 0.9059$ for maximum average output power and $R^2 = 0.8440$ for peak-stress prediction.

To determine the final neural-network architecture and training hyperparameters, sensitivity analyses were conducted for the hidden-layer size, dropout rate, and learning rate, as shown in Figure 3e–g. Increasing the number of hidden neurons improves the model representation capacity, but the validation loss reaches its minimum when the hidden layer contains approximately 398 neurons, indicating that further enlargement mainly increases model complexity without further reducing the validation loss. The dropout study identifies a dropout rate of 0.3 as the most effective regularization setting, while the learning-rate study shows that 2×10^{-3} provides a favorable balance between convergence speed and stability. The final network uses the pyramidal 398–199–99–49 hidden-layer widths. This engineering choice retains greater representation capacity near the input and progressively compresses features toward the output while reducing the parameter count in deeper layers. The four-layer depth was selected empirically before the sensitivity study, after which the first-layer width, dropout rate, and learning rate were tuned. Dropout is used as a regularization mechanism by randomly suppressing a fraction of activations during training, whereas the learning rate controls the optimizer step size and therefore the convergence speed and stability. The selected values were 398 neurons in the first hidden layer, a dropout rate of 0.3, and a learning rate of 2×10^{-3}.

Training robustness was additionally assessed using four random seeds (1, 7, 21, and 42) while keeping the training and validation datasets and all hyperparameters fixed. The seed-wise best validation MSE values had a mean and standard deviation of 0.1425 ± 0.0117, indicating limited sensitivity to initialization, mini-batch ordering, and Dropout randomness. The seed-wise best training and validation losses are shown in Figure S2 and discussed in Section S5. Because the training and validation datasets were fixed, this test evaluates training stochasticity rather than robustness to alternative independently sampled datasets.

2.4 | Genetic Algorithm Based Multi-Objective Inverse Design

To achieve an optimal trade-off between output power and stress concentration, this work integrates the trained neural network surrogate model with the non-dominated sorting genetic algorithm II (NSGA-II) to establish a multi-objective inverse optimization framework for auxetic piezoelectric energy harvesters, and the overall workflow is illustrated in Figure 4a. The optimization starts with the random initialization of an original population, where each individual corresponds to a set of structural geometric parameters defined by NURBS control points. Afterward, the trained ANN surrogate model is used to rapidly evaluate all candidate geometries within the population by predicting their maximum average output power and peak von Mises stress. These two quantities are directly adopted as the two objectives in the NSGA-II optimization, with the output power maximized and the peak stress minimized. The optimization is implemented using the Distributed Evolutionary Algorithms in Python (DEAP) framework, an open-source Python library for evolutionary computation. The corresponding fitness weights are set to $(1.0, -1.0)$, such that Pareto dominance is evaluated directly in the two-objective space rather than through a weighted-sum objective during the evolutionary process.

At each generation, the parent and offspring populations are combined and ranked according to Pareto non-dominance. A candidate is assigned to the first front if no other candidate is better in both objectives, with at least one objective being strictly better; subsequent fronts are obtained iteratively after removing the preceding fronts. Solutions with lower Pareto ranks are retained first. When the next front cannot be accommodated within the fixed population size, candidates are ranked by crowding distance, with larger values preferred to preserve solution diversity along the Pareto front. The evolutionary process therefore does not impose a subjective preference for a specific power–stress balance, but instead retains Pareto-efficient solutions spanning different trade-offs between output power and structural stress. Successive generations are generated through selection, crossover, and mutation until the predefined termination criteria are satisfied, after which representative configurations from the final Pareto solution set are further validated through FE simulations and experimental characterization.

The final NSGA-II configuration used a population size of 240 and 70 generations, with a crossover probability of 0.7 and a generation-level mutation probability of 0.15. Simulated binary crossover and polynomial mutation were used with distribution indices $\eta_c = 20$ and $\eta_m = 20$, respectively, and the per-variable mutation probability was 0.15. During the surrogate-driven evolutionary search, the explicit constraint handling was the prescribed lower and upper bounds of the 16 design variables. The resulting Pareto set is therefore interpreted as the surrogate-predicted non-dominated set within this bounded parameter domain. The optimization terminated after 70 generations; the supplementary hypervolume sensitivity analysis shows that the Pareto-front improvement was already close to a plateau by this point. After the NSGA-II search, the final OEH was selected from the non-dominated Pareto set as a compromise solution, balancing energy-harvesting performance and structural stress. As an independent check of surrogate accuracy at the final Pareto-selected design, the selected OEH was re-evaluated using the full finite-element model. The surrogate predicted a maximum average output power of 7.26 mW and a peak von Mises stress of 2.07 MPa, whereas the corresponding finite-element recalculation yielded 7.43 mW and 2.34 MPa, respectively. Using the finite-element results as the reference, the relative deviations were 2.29% for maximum average output power and 11.54% for peak von Mises stress. This comparison provides a direct surrogate-to-FE consistency check at the final selected Pareto solution. In contrast to conventional direct optimization relying on iterative finite element computation, the proposed surrogate-assisted optimization framework avoids massive repeated FE calculations throughout the evolutionary process, thereby reducing computational overhead while retaining favorable optimization accuracy and search efficiency. The developed methodology provides an efficient route for designing geometry-dominated auxetic energy harvesters.

21983844, 0, Downloaded from https://advanced.onlinelibrary.wiley.com/doi/10.1002/advs.78735 by Liuchao Jin , Wiley Online Library on [18/11/2026]. See the Terms and Conditions (https://onlinelibrary.wiley.com/terms-and-conditions) on Wiley Online Library for rules of use; OA articles are governed by the applicable Creative Commons License

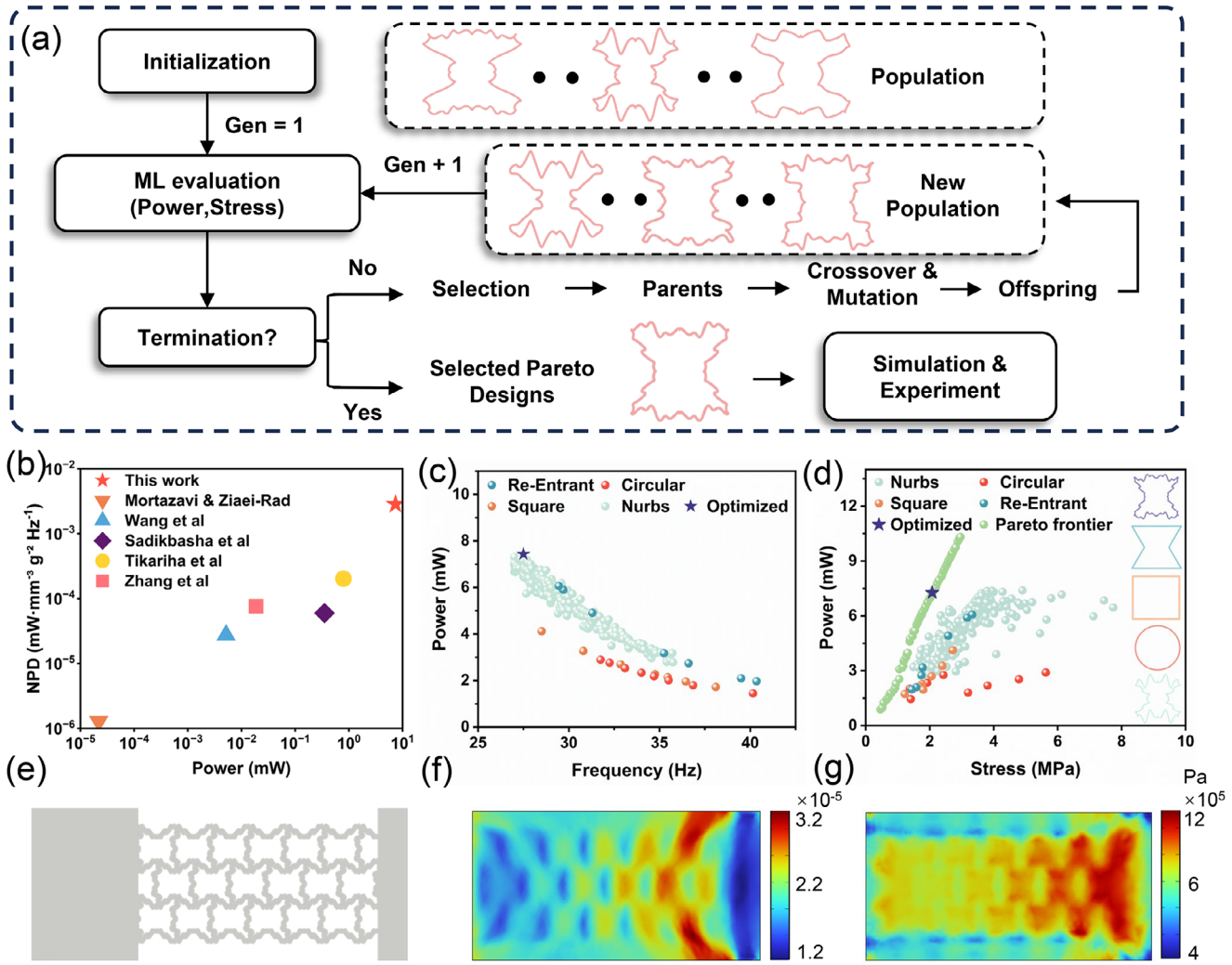


FIGURE 4 | Multi-objective optimization and performance evaluation of the auxetic piezoelectric energy harvester. (a) Workflow of the NSGA-II-based multi-objective optimization strategy integrated with the machine-learning surrogate model. The algorithm iteratively performs population initialization, fitness evaluation, selection, crossover, and mutation to obtain Pareto-optimal structural configurations balancing electrical power output and peak stress. (b) Comparison of normalized power density (NPD) between the present work and representative auxetic piezoelectric energy harvesters reported by Mortazavi & Ziaei-Rad [73], Wang et al. [74], Sadikbasha et al. [25], Tikariha et al. [75], and Zhang et al. [76]. (c) Resonant-frequency–output-power performance space of different structural configurations, including re-entrant, circular-hole, square-hole, NURBS-based, and optimized auxetic structures. Each point represents a distinct geometry evaluated at its corresponding resonant condition. (d) Pareto front distribution obtained from the multi-objective optimization process, illustrating the trade-off relationship between output power and peak von Mises stress for different geometric configurations. The optimized design achieves high electrical output while mitigating stress concentration. (e) Optimized auxetic substrate configuration obtained through the proposed inverse design framework. (f) Strain distribution of the optimized substrate under mechanical excitation. (g) Stress distribution of the piezoelectric layer in the optimized energy harvester, indicating a more uniform stress field and alleviated localized stress concentration after structural optimization.

To quantitatively benchmark the overall performance of the optimized configuration, Figure 4b compares the normalized power density (NPD) of the developed harvester with representative previously reported designs. In this work, NPD = $P/(Va^2f_r)$ where P (W) is the average output power, V (m^3) is the active piezoelectric-material volume, a (m s^{-2}) is the base-acceleration amplitude, and f_r (Hz) is the resonant frequency. For the present device, the active PZT volume is 372 mm^3 (60 mm × 31 mm × 0.2 mm), corresponding to the piezoelectric layer rather than the total device volume. For the literature comparison, active PZT volumes were taken from reported dimensions when available, and estimated values are explicitly indicated in Table S2. The optimized auxetic piezoelectric energy harvester yields milliwatt-level output power with a high normalized power density relative to the compared piezoelectric harvester designs. Particularly under low-frequency vibration excitations, the optimized structure sustains high energy harvesting capacity, demonstrating that the proposed geometry optimization strategy effectively improves the electromechanical conversion efficiency within low-frequency vibration environments. Compared to other types of auxetic piezoelectric energy harvesters, the normalized power density of this EH is improved. Such results support the benefit of combining auxetic topology with data-driven optimization for boosting energy harvesting performance. To clarify the perfor-

21983844, 0, Downloaded from https://advanced.onlinelibrary.wiley.com/doi/10.1002/advs.78735 by Liuchao Jin , Wiley Online Library on [18/11/2026]. See the Terms and Conditions (https://onlinelibrary.wiley.com/terms-and-conditions) on Wiley Online Library for rules of use; OA articles are governed by the applicable Creative Commons License

mance differences among diverse structural topologies, Figure 4c presents a resonant-frequency–output-power performance space formed by different geometries, including re-entrant, circular-hole, square-hole, NURBS-parameterized, and optimized configurations, rather than a frequency sweep of a single harvester. Each data point corresponds to a distinct geometry evaluated at its own resonant condition. Within the investigated design space, configurations with lower resonant frequencies generally exhibit higher output power, consistent with the larger vibration-induced deformation under the specified excitation and load conditions. Compared with conventional periodic hole-based architectures, the NURBS-parameterized structures access a broader range of low-frequency resonant and output-power combinations, demonstrating the greater design flexibility enabled by continuous geometric variation. As a representative experimental comparison, the resonance frequency shifts from 30.7 Hz for the pre-optimization NEH to 28.6 Hz for the OEH, while the OEH achieves a maximum average output power of 7.56 mW, exceeding that of the NEH under the same excitation condition. The distribution of candidate geometries therefore demonstrates that NURBS-based parameterization can effectively explore diverse low-frequency performance combinations, while the finalized optimized configuration achieves a high-power output at a low resonant frequency, highlighting its potential for low-frequency vibration energy harvesting. Figure 4d further depicts the quantitative correlation between output power and peak von Mises stress for all candidate configurations, where light-green scattered dots denote the Pareto-optimal solutions searched by NSGA-II. An inherent conflicting multi-objective characteristic is identified: the elevation of output power is generally accompanied by increased structural stress. Traditional circular-hole and square-hole layouts are mainly confined to the low-power region; although re-entrant auxetic structures produce relatively high power output, they suffer from excessive structural stress concentration. By contrast, NURBS parameterization expands the feasible design space via extra design freedoms and shifts the overall Pareto front toward the favorable high-power and low-stress zone. The ultimately selected optimal design lies in a favorable region of the Pareto front, achieving increased power output at a restricted stress level, which supports the capability of the established optimization framework to reconcile conflicting optimization objectives.

The optimized auxetic unit cell selected from the Pareto set is displayed in Figure 4e. In comparison with the initial prototype, the optimized unit cell possesses smooth, continuous curved boundaries. This morphology suggests that the optimization algorithm modulates local curvature and connecting domains to adjust the deformation pattern and electromechanical response. This outcome highlights that NURBS parameterization coupled with surrogate-assisted inverse optimization can access useful curved-geometry designs that are difficult to identify by empirical trial-and-error. To uncover the intrinsic enhancement mechanism behind the optimized performance, Figure 4f,g shows the strain and stress contours for the optimized harvester under operating excitations, respectively. The optimized topology effectively tailors internal load transfer paths and homogenizes mechanical deformation across the entire auxetic domain instead of accumulating deformation at narrow joint regions. The substrate layer presents expanded high-strain regions, enabling sufficient conversion from ambient vibrational energy into effective structural deformation; meanwhile, the stress distribution within piezoelectric layers becomes more uniform with clear mitigation of localized severe stress concentration. The combined effect of amplified effective strain and more homogeneous stress improves electromechanical conversion while providing a stress-distribution basis for reducing localized stress concentration.

In summary, the multi-objective inverse optimization framework couples a neural-network surrogate model with NSGA-II to identify structural configurations that balance high output power and low peak stress in a nonlinear design space. The optimized auxetic piezoelectric energy harvester exhibits enhanced energy-harvesting performance under low-frequency excitation while mitigating localized stress concentration. The proposed inverse-design methodology supports the development of stress-aware self-powered wireless sensing nodes for long-term structural and industrial monitoring.

2.5 | Experimental Validation of the Optimized Energy Harvester

The experimental setup, shown in Figure 5a, was established to characterize the electromechanical performance of the fabricated energy harvesters. The devices under test included a conventional piezoelectric energy harvester (PEH), an auxetic hexagonal-structured piezoelectric energy harvester (AEH), a NURBS-based auxetic piezoelectric energy harvester (NEH), and the optimized energy harvester (OEH). The system comprised a shaker, a power amplifier, and a vibration controller. The power amplifier belonged to the excitation chain, which amplified the low-level controller signal to provide the voltage and current required to drive the electrodynamic shaker and maintain the prescribed base acceleration. Each harvester prototype was rigidly fixed to the shaker table, which provided a controllable base excitation. The piezoelectric output terminals were connected to a precision resistor box for load resistance adjustment, and the output voltage was recorded using a digital oscilloscope. All measurements were conducted under laboratory conditions with constant temperature and humidity to ensure the repeatability and reliability of the results.

To investigate the resonance characteristics and voltage output performance, frequency sweep experiments were performed. The base acceleration amplitude was maintained at a constant 0.5g (approximately 4.9 m/s^2), and the open-circuit peak voltage was recorded as a function of the excitation frequency, as presented in Figure 5b. The resonance frequencies of the PEH, AEH, NEH, and OEH configurations were experimentally identified as approximately 80, 35.5, 30.7, and 28.6 Hz, respectively. The experimental and numerical results show consistent resonant locations and peak-voltage trends, supporting the dynamic and electrical consistency of the multiphysics finite-element model. The local peak-stress field was not directly measured experimentally; consequently, peak von Mises stress is used in this study as a model-based comparative indicator of stress concentration rather than as an experimentally calibrated failure criterion.

As further quantified in Figure S4, the relative error in peak voltage between the simulations and experiments is at most approximately 10%, while the maximum deviation in resonant frequency

21983844, 0, Downloaded from https://advanced.onlinelibrary.wiley.com/doi/10.1002/advs.78735 by Liuchao Jin , Wiley Online Library on [18/11/2026]. See the Terms and Conditions (https://onlinelibrary.wiley.com/terms-and-conditions) on Wiley Online Library for rules of use; OA articles are governed by the applicable Creative Commons License

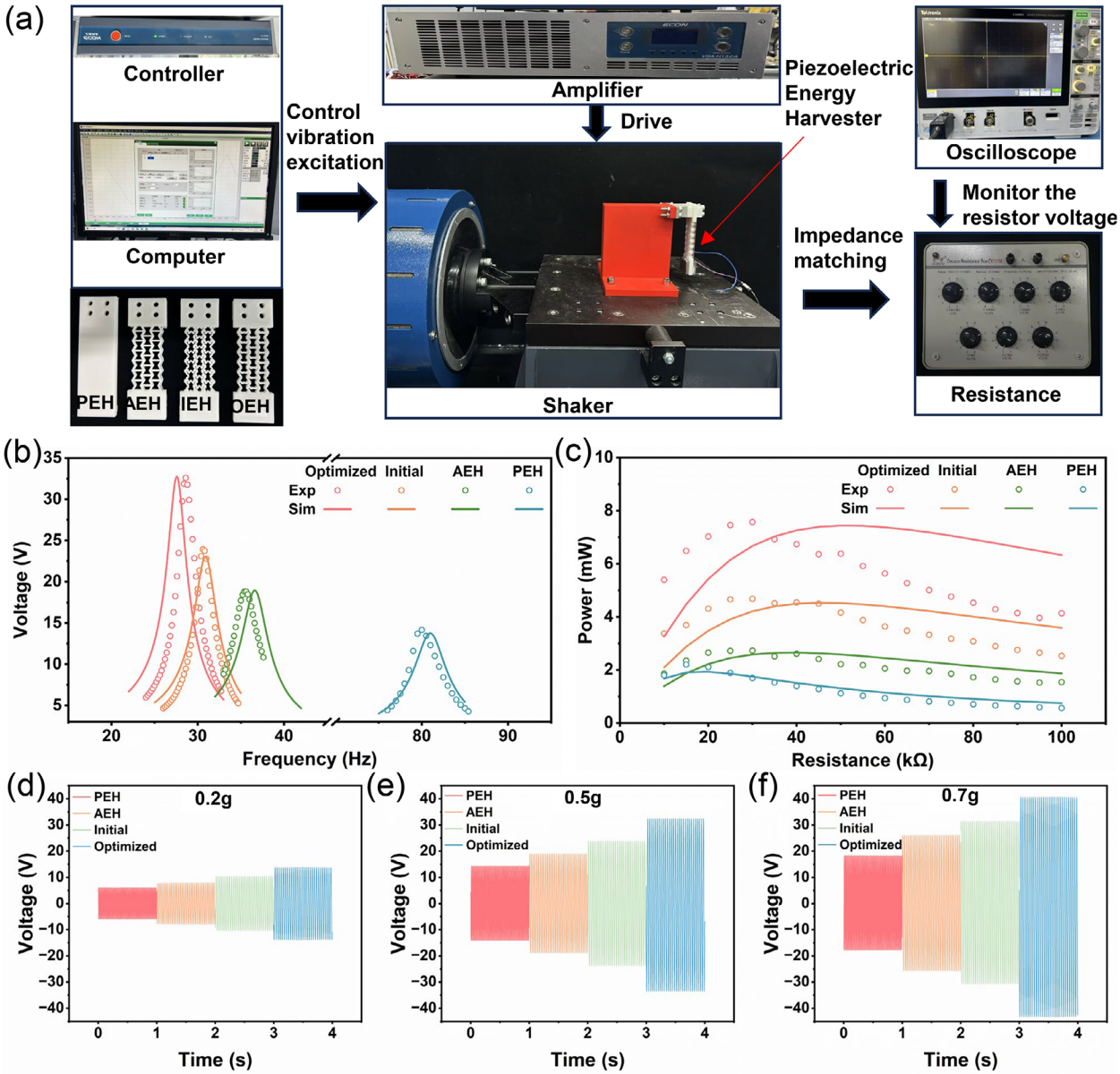


FIGURE 5 | Experimental validation of the optimized auxetic energy harvesters. (a) Experimental setup showing the shaker, amplifier, controller, oscilloscope, and test specimens (PEH, AEH, NEH, OEH). (b) Frequency-dependent open-circuit voltage for each harvester. (c) Output power versus load resistance, highlighting optimal resistance for maximum power. (d-f) Time-domain voltage responses under base accelerations of 0.2g (d), 0.5g (e), and 0.7g (f), demonstrating enhanced output of the optimized design.

is 2.1 Hz. These discrepancies may arise from several sources, including 3D-printing tolerances, uncertainties in the elastic and piezoelectric material properties, variations in adhesive-layer thickness and bonding conditions, non-ideal clamping, uncertainty in damping parameters, electronic-component tolerances, and the idealized linear-material and boundary assumptions adopted in the numerical model. Because the surrogate model is trained exclusively on finite-element data, any systematic bias inherent to the FE model may also propagate into its absolute predictions. Nevertheless, the numerical model reproduces the primary trends in resonant frequency and output voltage across different geometries, and the final OEH is independently validated through both FE simulation and experimental characterization. Accordingly, the FE dataset is used primarily to learn relative geometry–performance relationships and guide the optimization process, rather than to imply exact experimental-level prediction accuracy for every candidate geometry.

The in-plane average normal stresses summarized in Table 3 provide a quantitative explanation for the enhanced electrical output of the optimized configuration. It should be noted that the stress objective used in the optimization is the peak von Mises stress, which is dominated by localized stress concentrations, whereas the quantities reported in Table 3 are spatially averaged in-plane normal stresses in the piezoelectric layer. Here, $\bar{\sigma}_{11}$ and $\bar{\sigma}_{22}$ denote the spatially averaged longitudinal and transverse stresses in the piezoelectric layer, respectively. These metrics therefore characterize different aspects of the stress field and should not be expected to vary in the same manner. By modifying the local curvature and load-transfer pathways, the optimized geometry

21983844, 0, Downloaded from https://advanced.onlinelibrary.wiley.com/doi/10.1002/advs.78735 by Liuchao Jin , Wiley Online Library on [18/11/2026]. See the Terms and Conditions (https://onlinelibrary.wiley.com/terms-and-conditions) on Wiley Online Library for rules of use; OA articles are governed by the applicable Creative Commons License

TABLE 3 | Comparison of in-plane average normal stresses in the piezoelectric layer for different energy harvesters.

Energy harvester	$\bar{\sigma}_{11}$ (MPa)	$\bar{\sigma}_{22}$ (MPa)
OEH	−0.47704	−0.18750
NEH	−0.36305	−0.11609
AEH	−0.28308	−0.09177
PEH	−0.10054	0.00643

redistributes deformation over a larger active PZT region, thereby mitigating severe local stress concentrations while increasing the average longitudinal and transverse stress components that contribute to piezoelectric conversion. Compared with the PEH, AEH, and NEH, the optimized design consequently exhibits larger-magnitude average in-plane stresses in the piezoelectric layer, indicating more effective stress transfer and a stronger electromechanical driving state. Thus, the optimized configuration does not simply reduce the overall stress level; rather, it simultaneously suppresses the most severe local stress hotspots targeted by the optimization and enhances the spatially distributed stress contribution relevant to electrical energy conversion.

Impedance matching experiments were conducted to determine the optimal load resistance for maximizing the average output power of each harvester. Each device was excited at its respective resonance frequency with a constant base acceleration of 0.5g (approximately 4.9 m s^{-2}). The load resistance was varied from near-short-circuit conditions to 100 kΩ using the precision resistor box. The root-mean-square (RMS) voltage across the load was recorded, and the corresponding output power was calculated using $P = V_{\mathrm{RMS}}^2/R$. The resulting power–resistance curves are shown in Figure 5c. The optimized harvester (OEH) achieved a maximum average output power of 7.56 mW at its optimal load resistance, exceeding the NEH configuration and confirming the effectiveness of the optimization strategy.

To evaluate the dynamic response under different excitation intensities, constant-frequency excitation experiments were performed. Each harvester was driven at its respective resonance frequency under base acceleration levels of 0.2g, 0.5g, and 0.7g. The time-domain voltage responses were recorded, as illustrated in Figure 5d–f. For all harvesters, the peak output voltage increased with increasing excitation acceleration. Notably, at an excitation of 0.7g, the optimized harvester delivered a peak output voltage of 40 V, substantially higher than those of the PEH and AEH, demonstrating enhanced electromechanical conversion efficiency. Collectively, these experimental results confirm that the optimized design effectively enhances the output performance of the energy harvester under various vibration conditions.

2.6 | System-Level Demonstration: Self-Powered LoRa Sensing

To evaluate practical energy autonomy, the vibration energy harvester was integrated with a wireless Internet-of-Things (IoT) sensing node to form a vibration-powered sensing system (VPSS). The complete energy-to-communication pathway, from vibration energy harvesting and storage to wireless data transmission, was experimentally evaluated to assess how the structural optimization translates into system-level operation. The wireless communication module employs LoRa (Long Range), a low-power wide-area wireless communication technology designed for long-range data transmission with low energy consumption. The VPSS comprises an energy harvesting and storage stage, threshold-triggered power management, temperature sensing, LoRa-based wireless transmission, and remote data reception, thereby enabling the harvested energy to support sensing and wireless communication without an external power supply.

Figure 6a presents the complete hardware architecture schematic of the VPSS. The platform is divided into four electrically coupled modules: the energy enhancement unit (EEU), energy management unit (EMU), energy utilization unit (EUU), and LoRa communication unit. As illustrated in Figure 6b, these functional units are physically integrated onto a compact printed circuit board (PCB). The EEU uses a low-forward-voltage full-bridge rectifier to convert the harvester's AC output into rectified DC, which is then stored in a capacitor. The EMU acts as the central power-management and control unit. It is built around a Nordic nRF52-series microcontroller and integrates a voltage comparator, electrically erasable programmable read-only memory (EEPROM), and buck-converter control circuitry. The voltage comparator monitors the capacitor voltage and determines whether predefined voltage thresholds have been reached, while the microcontroller uses this information to control the power-delivery sequence and activate the downstream loads at the appropriate operating conditions. The EEPROM stores the system parameters and configuration information required for system operation. The EUU contains the low-power sensing load, including a temperature sensor, which is powered by the EMU according to the predefined control sequence. Once the sensing operation is completed, the acquired temperature data are processed by the microcontroller and transmitted through an SX1276 LoRa transceiver to a remote receiver. Thus, the four modules collectively establish an energy flow from AC harvesting and rectification to energy storage, voltage-dependent power management, environmental sensing, and wireless data transmission, enabling autonomous operation without an external power supply.

To emulate self-powered wireless sensing under realistic operating conditions, the experimental environment depicted in Figure 6c was constructed. A vibration shaker, driven under a constant acceleration excitation of 0.5g (approximately 4.9 m s^{-2}), was employed to provide a stable and controllable vibration energy input. The vibration driving system, the energy harvester, and the VPSS sensing node were deployed within an indoor laboratory setting, whereas the LoRa signal receiving terminal was positioned outdoors at a distance of approximately 150 m from the transmitter (Video S1). This configuration was designed to verify the long-range communication capability of the system under non-line-of-sight (NLOS) conditions. The NURBS-based harvester (NEH) and optimized harvester (OEH) were used as front-end vibration harvesters to compare their effects on VPSS operation. The intermittent operation of the VPSS is governed by the EMU hardware voltage threshold of 5.0 V. The system operates in four sequential phases: energy accumulation, threshold triggering, voltage conversion/load powering, and data transmis-

21983844, 0, Downloaded from https://advanced.onlinelibrary.wiley.com/doi/10.1002/advs.78735 by Liuchao Jin , Wiley Online Library on [18/11/2026]. See the Terms and Conditions (https://onlinelibrary.wiley.com/terms-and-conditions) on Wiley Online Library for rules of use; OA articles are governed by the applicable Creative Commons License

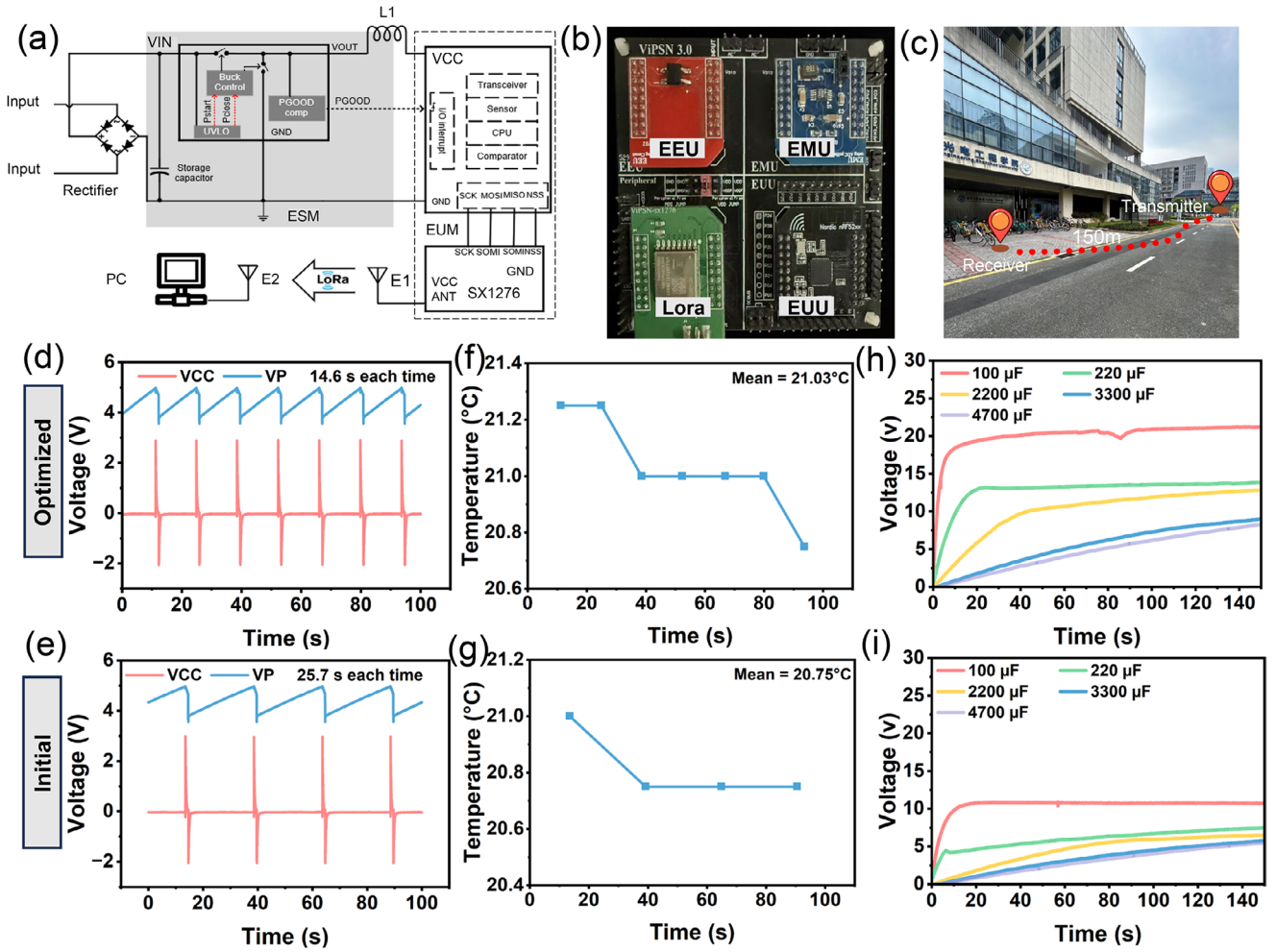


FIGURE 6 | System-level demonstration of self-powered LoRa sensing using the optimized energy harvester. (a) Hardware architecture schematic showing EEU, EMU, EUU, and LoRa communication units. (b) Photograph of the integrated PCB with functional modules. (c) Indoor-to-outdoor experimental setup illustrating a 150 m LoRa transmission. (d, e) Time-domain voltage waveforms of storage capacitor (V_P) and system supply (V_{CC}) for the OEH (d) and NEH (e) harvesters. (f, g) Corresponding temperature data received during operation for OEH (f) and NEH (g). (h, i) Charging voltage of storage capacitors with different capacitances for OEH (h) and NEH (i), demonstrating enhanced energy accumulation of the optimized harvester.

sion. During energy accumulation, the harvester outputs an AC voltage under vibration excitation, which is rectified by the EEU to charge the storage capacitor and increase the capacitor voltage V_P. Throughout this period, the EMU keeps the downstream EUU and LoRa unit electrically isolated, maintaining the system in an ultra-low-power sleep mode.

Once V_P reaches the preset threshold of 5.0 V, the threshold-triggering phase begins. The internal voltage comparator of the EMU generates a toggle signal that wakes the CPU and initiates the pre-programmed control routine. The integrated DC–DC buck converter is then activated to regulate V_P from 5.0 to 3.3 V and deliver a stable operating voltage, V_{CC}, to the LoRa module and the temperature sensor. In this phase, V_{CC} rises from a standby level of approximately 0.2 to 3.2 V, indicating successful activation of the downstream load circuitry. During data acquisition and wireless transmission, the temperature data are read and processed by the nRF52-series microcontroller, which communicates with the SX1276 LoRa transceiver through a Serial Peripheral Interface (SPI) bus and transfers the acquired data for wireless transmission. The LoRa module then encapsulates the data into frames and transmits them through the on-board antenna. After a single transmission task, V_P drops below the threshold level due to the rapid release of stored charge, prompting the EMU to disconnect the load power supply path and return the system to the energy accumulation state. This cycle constitutes one intermittent self-powered operating period of the VPSS.

To quantitatively evaluate the system-level benefit of structural optimization, the key node voltage waveforms and temperature data transmission of the VPSS were recorded under identical vibration excitation conditions (0.5g, approximately 4.9 m s^{-2}), using the OEH and NEH as front-end harvesters, respectively. A 2200 μF storage capacitor was used for the seven-cycle OEH and four-cycle NEH comparison. The wireless communication module was based on an SX1276 transceiver operating at 433 MHz with a transmission power of 14 dBm, and the sensing data were packaged into a 12-byte payload for transmission. Figure 6d presents the typical time-series waveforms of V_P and V_{CC} during system operation with the OEH configuration. The energy accumulation time required for V_P to charge from the initial state to

21983844, 0, Downloaded from https://advanced.onlinelibrary.wiley.com/doi/10.1002/advs.78735 by Liuchao Jin , Wiley Online Library on [18/11/2026]. See the Terms and Conditions (https://onlinelibrary.wiley.com/terms-and-conditions) on Wiley Online Library for rules of use; OA articles are governed by the applicable Creative Commons License

the threshold voltage of 5.0 V was approximately 14.6 s. Within the observed 100 s time window, V_P underwent seven complete charge–discharge cycles. Each abrupt drop in V_P was synchronized with a corresponding step rise in V_{CC}, indicating that the EMU successfully triggered seven load-powering operations.

In direct contrast, Figure 6e illustrates the system response when employing the NEH structure. Within the same observation window, the charging rate of V_P was significantly slower, with a single charge cycle extending to approximately 25.7 s, resulting in only four complete charge–discharge cycles within 100 s. These results demonstrate that, owing to its higher output power density under identical excitation conditions, the OEH accumulates the energy required to reach the capacitor threshold voltage within a shorter time interval, thereby enabling periodic self-powered temperature transmission with a higher sensing-transmission frequency.

Figure 6f,g shows the discrete temperature data points received on the PC interface for the OEH and NEH structures. With the OEH structure (Figure 6f), seven valid temperature data packets were successfully received and demodulated within 100 s, with an average temperature of 21.02°C. With the NEH structure (Figure 6g), only four valid temperature data packets were received and demodulated during the same period, with an average temperature of 20.75°C. The time intervals between the received data points were highly consistent with the step periods of V_{CC} shown in Figure 6d and 6e, further verifying the temporal consistency of the VPSS energy management logic.

Figure 6h,i depicts the voltage evolution of storage capacitors with different nominal capacitances as a function of charging time, using the OEH and NEH structures as the front-end harvesters, respectively. The selected capacitance values were 100, 220, 2200, 3300, and 4700 μF. The capacitor-charging tests in Figure 6h,i were conducted without EMU threshold-triggered discharge so that the intrinsic charging capability of the harvesters could be compared under different capacitances. As shown in Figure 6h, under the constant input power condition provided by the OEH structure, the terminal voltages of all capacitors exhibited a rapid initial rise followed by a gradual slowdown. The 100 μF capacitor exhibited the fastest voltage rise, followed by the 220 μF capacitor. In contrast, the 3300 and 4700 μF capacitors showed markedly lower voltage-rise slopes within the 140 s observation window. The test results for the NEH structure shown in Figure 6i exhibited the same general trend but lower charging rates because of the lower output power of the NEH.

In summary, the system-level demonstration experiments validated the feasibility of self-powered environmental temperature sensing and 150 m LoRa wireless data transmission using the VPSS. Compared with the control NEH structure, the optimized OEH shortened the charging time and increased the number of completed sensing-transmission cycles. The modular hardware architecture, combined with the threshold-voltage-based intermittent energy management strategy, provides a practical reference for the design of low-power self-powered wireless sensing nodes for ubiquitous sensor networks and Industrial Internet of Things (IIoT) applications.

3 | Conclusions

This study presents a surrogate-assisted inverse-design framework for auxetic piezoelectric energy harvesters that integrates compact NURBS-based geometric parameterization, neural-network surrogate modeling, and NSGA-II multi-objective optimization to address the power–stress-concentration trade-off.

The methodological contribution lies in integrating NURBS, neural networks, NSGA-II, and LoRa into a continuous, stress-aware multi-objective inverse-design workflow for auxetic piezoelectric energy harvesters. In this framework, NURBS defines the optimization-compatible geometric design space, the neural network provides rapid forward prediction of power and peak stress, NSGA-II explores the corresponding power–stress Pareto trade-off, and the LoRa platform serves as application-level validation of the selected optimized harvester. The adopted NURBS representation enables systematic exploration of curved re-entrant auxetic geometries through a fixed set of physically interpretable control-point variables while preserving geometric continuity.

Finite element simulations show that the NURBS-governed auxetic substrate improves the deformation and stress/strain fields relative to the conventional solid substrate and the straight internal-hexagon auxetic substrate. The NURBS configuration increases the free-end displacement along longitudinal direction, promotes transverse expansion with the same sign as the longitudinal strain, extends the active stress region in the piezoelectric layer, and improves strain uniformity. These changes support biaxial strain amplification and reduce stress localization, which together enhance electromechanical conversion. To reduce the cost of exhaustive finite-element parameter sweeps, a feedforward neural-network surrogate model is trained on a Latin-hypercube-sampled simulation dataset. The surrogate model exhibits good predictive accuracy within the sampled design space, achieving coefficients of determination (R^2) of 0.9059 and 0.8440 for maximum average output power and peak-stress prediction, respectively. By coupling this surrogate model with the NSGA-II multi-objective genetic algorithm, a Pareto frontier is successfully identified, explicitly revealing the intrinsic competition between maximizing output power and minimizing peak stress. The selected optimized configuration sustains high electrical output while mitigating localized high-stress concentrations.

Experimental validation corroborates the numerical findings. Under a base excitation of 0.5g (approximately 4.9 $\mathrm{m\,s^{-2}}$), the optimized energy harvester delivers a maximum average output power of 7.56 mW, corresponding to a normalized power density of 2.84×10^{-3} $\mathrm{mW/(mm^3 \cdot g^2 \cdot Hz)}$, which is competitive with comparable piezoelectric vibration energy harvesters. Furthermore, the practical viability of the proposed methodology is demonstrated through the implementation of a self-powered LoRa wireless sensing system. The optimized harvester achieves seven complete charge–discharge cycles within a 100 s observation window, supporting seven valid temperature data transmissions over a 150 m communication link, representing a 75% increase in the number of completed sensing-transmission cycles compared with the NEH configuration. The modular hardware architecture, combined with the threshold-voltage-based inter-

21983844, 0, Downloaded from https://advanced.onlinelibrary.wiley.com/doi/10.1002/advs.78735 by Liuchao Jin , Wiley Online Library on [18/11/2026]. See the Terms and Conditions (https://onlinelibrary.wiley.com/terms-and-conditions) on Wiley Online Library for rules of use; OA articles are governed by the applicable Creative Commons License

mittent energy management strategy, provides a scalable technical reference for the design of low-power self-powered wireless sensing nodes. Overall, this work connects inverse auxetic-geometry design, stress-aware piezoelectric energy harvesting, and self-powered LoRa sensing, providing a practical route toward battery-independent IoT and industrial monitoring nodes.

Acknowledgements

Shitong Fang acknowledges the support by National Natural Science Foundation of China (Grant No. 52575130), Guangdong Basic and Applied Basic Research Foundation (Grant No. 2026A1515010148), and Shenzhen Natural Science Fund (Grant No. JCYJ20230808105206013). Wei-Hsin Liao acknowledges the support by Hong Kong Research Grants Council (CUHK 14211823 and SRFS2627-4S01), and The Chinese University of Hong Kong (Project No. 4055310). Liuchao Jin acknowledges the support by the Hong Kong Research Grants Council under the Hong Kong PhD Fellowship Scheme (No. PF21-60853).

Conflicts of Interest

The authors declare no potential conflicts of interest with respect to the research, authorship, and/or publication of this article.

Data Availability Statement

The data that support the findings of this study are available from the corresponding author upon reasonable request.

References

1. A. Ali, S. Iqbal, and X. Chen, "Recent Advances in Piezoelectric Wearable Energy Harvesting Based on Human Motion: Materials, Design, and Applications," *Energy Strategy Reviews* 53 (2024): 101422.

2. L. Qi, L. Kong, Y. Wang, et al., "Recent Progress in Application-Oriented Self-Powered Microelectronics," *Advanced Energy Materials* 13, no. 47 (2023): 2302699.

3. L. Xiao, B. Yin, Z. Geng, J. Li, R. Jia, and K. Zhang, "Flexible Wearable Devices Based on Self-Powered Energy Supply," *Nano Energy* 142 (2025): 111157.

4. L.-C. Zhao, H.-X. Zou, K.-X. Wei, S.-X. Zhou, G. Meng, and W.-M. Zhang, "Mechanical Intelligent Energy Harvesting: From Methodology to Applications," *Advanced Energy Materials* 13, no. 29 (2023): 2300557.

5. S. Fang, H. Peng, M. Cai, et al., "Gecko-Like Multi-Directional High-Power Magneto–Mechano–Electric Energy Harvesters for Self-Powered, Hundred-Meter-Scale LoRa Communication," *Advanced Science* 13, no. 32 (2026): e74974.

6. L. Zhao, Z. Chen, X. Chen, et al., "Design and Analysis of a Mechanically Intelligent System for Biomechanical Energy Harvesting," *Applied Mathematics and Mechanics* 47, no. 2 (2026): 235–254.

7. L.-C. Zhao, Z.-W. Chen, Q.-H. Gao, et al., "Self-Aligning Mechanism for Wearable Biomechanical Energy Harvesters," *Device* 4, no. 1 (2026): 100972.

8. A. Luo, Q. Tan, W. Xu, et al., "A Comprehensive Review of Energy Harvesting From Kinetic Energy at Low Frequency," *Advanced Materials Technologies* 10, no. 13 (2025): 2401731.

9. B. Mahanty, S. K. Ghosh, and D.-W. Lee, "Advancements in Polymer Nanofiber-Based Piezoelectric Nanogenerators: Revolutionizing Self-Powered Wearable Electronics and Biomedical Applications," *Chemical Engineering Journal* 495 (2024): 153481.

10. Q. He and J. Briscoe, "Piezoelectric Energy Harvester Technologies: Synthesis, Mechanisms, and Multifunctional Applications," *ACS Applied Materials & Interfaces* 16, no. 23 (2024): 29491–29520.

11. Q. Gao, Y. Lu, Y. Shi, et al., "Enhancing the Output Performance of Energy Harvesters Using Hierarchical Auxetic Structure and Optimization Techniques," *IEEE Transactions on Industrial Electronics* 71, no. 9 (2023): 11641–11649.

12. M. Ravanbod and S. Ebrahimi-Nejad, "Perforated Auxetic Honeycomb Booster With Reentrant Chirality: A New Design for High-Efficiency Piezoelectric Energy Harvesting," *Mechanics of Advanced Materials and Structures* 31, no. 27 (2024): 9857–9872.

13. A. Tabak, B. Safaei, A. Memarzadeh, S. Arman, and C. Kizilors, "An Extensive Review of Piezoelectric Energy-Harvesting Structures Utilizing Auxetic Materials," *Journal of Vibration Engineering & Technologies* 12, no. 3 (2024): 3155–3192.

14. X. Zhang, Y. Yu, X. Xia, et al., "Multi-Mode Vibrational Triboelectric Nanogenerator for Broadband Energy Harvesting and Utilization in Smart Transmission Lines," *Advanced Energy Materials* 13, no. 43 (2023): 2302353.

15. X. Zhou, K. Parida, J. Chen, et al., "3D Printed Auxetic Structure-Assisted Piezoelectric Energy Harvesting and Sensing," *Advanced Energy Materials* 13, no. 34 (2023): 2301159.

16. H. Choi, B.-K. Min, S.-J. Joo, et al., "Partially Air-Filled Skin-Attachable Deformable Gasket with Negative Poisson's Ratio for Highly-Efficient Stretchable Thermoelectric Generators," *Advanced Energy Materials* 13, no. 40 (2023): 2301252.

17. O. Yue, X. Wang, Y. Zhou, et al., "Auxetic Structure-Assisted Triboelectric Nanogenerators for Efficient Energy Collection and Wearable Sensing," *Advanced Energy Materials* 14, no. 24 (2024): 2400212.

18. K. Chen, S. Fang, Z. Lai, J. Cao, and W.-H. Liao, "A Plucking Rotational Energy Harvester With Tapered Thickness and Auxetic Structures for Increasing Power Output," *Applied Energy* 357 (2024): 122490.

19. K. Chen, Q. Gao, S. Fang, D. Zou, Z. Yang, and W.-H. Liao, "An Auxetic Nonlinear Piezoelectric Energy Harvester for Enhancing Efficiency and Bandwidth," *Applied Energy* 298 (2021): 117274.

20. Q. Li, Y. Kuang, and M. Zhu, "Auxetic Piezoelectric Energy Harvesters for Increased Electric Power Output," *AIP Advances* 7, no. 1 (2017): 015104.

21. P. Eghbali, D. Younesian, and S. Farhangdoust, "Enhancement of Piezoelectric Vibration Energy Harvesting With Auxetic Boosters," *International Journal of Energy Research* 44, no. 2 (2020): 1179–1190.

22. K. Chen, S. Fang, Q. Gao, D. Zou, J. Cao, and W.-H. Liao, "An Enhanced Nonlinear Piezoelectric Energy Harvester With Multiple Rotating Square Unit Cells," *Mechanical Systems and Signal Processing* 173 (2022): 109065.

23. M. L. De Bellis and A. Bacigalupo, "Auxetic Behavior and Acoustic Properties of Microstructured Piezoelectric Strain Sensors," *Smart Materials and Structures* 26, no. 8 (2017): 085037.

24. P. Eghbali, D. Younesian, A. Moayedizadeh, and M. Ranjbar, "Study in Circular Auxetic Structures for Efficiency Enhancement in Piezoelectric Vibration Energy Harvesting," *Scientific Reports* 10, no. 1 (2020): 16338.

25. S. Sadikbasha, B. Radhika, and V. Pandurangan, "Auxetic Hexachiral Cantilever Beams for Piezoelectric Vibration Energy Harvesting," *Smart Materials and Structures* 31, no. 10 (2022): 105015.

26. X. Zhang, X. Shan, G. Sui, et al., "Enhancing Piezoelectric Energy Harvesters With Rotating Triangular Auxetic Structures," *International Journal of Mechanical Sciences* 289 (2025): 110081.

27. Y.-H. Yeh, D. T. Lin, and K.-D. Li, "Optimization of ZnO Piezoelectric Properties: Effects of Spin-Coating Parameters on Microstructure and Performance," *Journal of Electronic Materials* 54, no. 7 (2025): 5178–5188.

28. K. Meinel, M. Melzer, C. Stoeckel, et al., "2D Scanning Micromirror With Large Scan Angle and Monolithically Integrated Angle Sensors Based on Piezoelectric Thin Film Aluminum Nitride," *Sensors* 20, no. 22 (2020): 6599.

29. A. Ivanoska-Dacikj, P. Makreski, S. Sukumaran, and U. Stachewicz, "Design of Experiments as a Comprehensive Framework to Optimize

21983844, 0, Downloaded from https://advanced.onlinelibrary.wiley.com/doi/10.1002/advs.78735 by Liuchao Jin , Wiley Online Library on [18/11/2026]. See the Terms and Conditions (https://onlinelibrary.wiley.com/terms-and-conditions) on Wiley Online Library for rules of use; OA articles are governed by the applicable Creative Commons License

Electrospinning Parameters for Enhanced β-Phase in Poly (vinylidene fluoride-co-hexafluoropropylene)," *Journal of Polymer Research* 32, no. 9 (2025): 303.

30. A. Kumar, M. Prasad, V. Janyani, and R. Yadav, "Fabrication and Annealing Temperature Optimization for a Piezoelectric ZnO Based MEMS Acoustic Sensor: Kumar, Prasad, Janyani, and Yadav," *Journal of Electronic Materials* 48, no. 9 (2019): 5693–5701.

31. M. Öztürk, T. Baran, and M. S. Tatlıer, "Experimental and Numerical Investigation of Conventional and Stiffened Re-Entrant Cell Structures Under Compression," *Journal of the Brazilian Society of Mechanical Sciences and Engineering* 44, no. 12 (2022): 593.

32. H.-G. Choi, S. Pyo, J.-W. Choi, and K. Park, "Shape Morphing of Re-Entrant Honeycomb Metamaterials for Linear Auxetic Behaviors," *Advanced Engineering Materials* 27, no. 1 (2025): 2400889.

33. H. Ohtaki, G. Hu, Y. Nagasaka, and S. Kotosaka, "Analysis of Negative Poisson's Ratios of Re-Entrant Honeycombs," *JSME International Journal Series A Solid Mechanics and Material Engineering* 47, no. 2 (2004): 113–121.

34. M. Fu, O. Xu, L. Hu, and T. Yu, "Nonlinear Shear Modulus of Re-Entrant Hexagonal Honeycombs Under Large Deformation," *International Journal of Solids and Structures* 80 (2016): 284–296.

35. R. Brighenti, A. Spagnoli, M. Lanfranchi, and F. Soncini, "Nonlinear Deformation Behaviour of Auxetic Cellular Materials With Re-Entrant Lattice Structure," *Fatigue & Fracture of Engineering Materials & Structures* 39, no. 5 (2016): 599–610.

36. A. H. Tajalsir, K. Mustapha, and T. Ibn-Mohammed, "Numerical and Random Forest Modelling of the Impact Response of Hierarchical Auxetic Structures," *Materials Today Communications* 31 (2022): 103797.

37. F. Luo, S. Zhang, and D. Yang, "Anti-Explosion Performance of Composite Blast Wall With an Auxetic Re-Entrant Honeycomb Core for Offshore Platforms," *Journal of Marine Science and Engineering* 8, no. 3 (2020): 182.

38. H. Wu, R. Zhong, W. Chen, and M. Fu, "A Novel Mechanical Metamaterial With Dramatically Different Elastic Parameters in Tension and Compression," *Materials Today Communications* 34 (2023): 105385.

39. Y. Wang, Q. He, Y. Chen, H. Gu, and H. Zhou, "In-Plane Dynamic Crushing of a Novel Bio-Inspired Re-Entrant Honeycomb With Negative Poisson's Ratio," *Journal of the Brazilian Society of Mechanical Sciences and Engineering* 43, no. 10 (2021): 461.

40. J. Choi and R. Lakes, "Nonlinear Analysis of the Poisson's Ratio of Negative Poisson's Ratio Foams," *Journal of Composite Materials* 29, no. 1 (1995): 113–128.

41. K. El Nady, F. Dos Reis, and J. Ganghoffer, "Computation of the Homogenized Nonlinear Elastic Response of 2D and 3D Auxetic Structures Based on Micropolar Continuum Models," *Composite Structures* 170 (2017): 271–290.

42. C. Qian and W. Ye, "Accelerating Gradient-Based Topology Optimization Design With Dual-Model Artificial Neural Networks: Accelerating Gradient-Based Topology Optimization Design With Dual-Model Artificial Neural Networks," *Structural and Multidisciplinary Optimization* 63, no. 4 (2021): 1687–1707.

43. S. Bilicz, M. Lambert, S. Gyimothy, and J. Pavo, "Solution of Inverse Problems in Nondestructive Testing by a Kriging-Based Surrogate Model," *IEEE Transactions on Magnetics* 48, no. 2 (2012): 495–498.

44. A. Torregrosa, L. García-Cuevas, P. Quintero, and A. Cremades, "On the Application of Artificial Neural Network for the Development of a Nonlinear Aeroelastic Model," *Aerospace Science and Technology* 115 (2021): 106845.

45. S. M. A. Rahmati, M. Rostami, and A. Karimi, "A Novel Optimization Framework to Improve the Computational Cost of Muscle Activation Prediction for a Neuromusculoskeletal System," *Neural Computation* 31, no. 3 (2019): 574–595.

46. L. Zhou, S. S. Menon, X. Li, M. Zhang, and M. H. Malakooti, "Machine Learning Enables Reliable Colorimetric Detection of pH and Glucose in Wearable Sweat Sensors," *Advanced Materials Technologies* 10, no. 3 (2025): 2401121.

47. J. Wang, L. Jin, Q. Gao, and W.-H. Liao, "Graded Infill Design of Thin-Walled Structures With Connectable Nonuniform Microstructures Based on the Data-Driven Surrogate Model," *Thin-Walled Structures* 231 (2026): 115426.

48. S. Fang, H. Lin, A. Ye, et al., "Machine Learning-Enabled Inverse Design of Heterogeneous Impact-Resistant Metamaterials," *International Journal of Mechanical Sciences* 329 (2026): 112110.

49. A. Zolfagharian, L. Jin, Q. Ge, et al., "Roadmap on Artificial Intelligence-Augmented Additive Manufacturing," *Advanced Intelligent Systems* 8, no. 4 (2026): e202500484.

50. L. Jin, X. Zhai, K. Wang, et al., "Big Data, Machine Learning, and Digital Twin Assisted Additive Manufacturing: A Review," *Materials & Design* 244 (2024): 113086.

51. L.-H. Yang, X.-L. Luo, Z.-B. Yang, C.-F. Nan, X.-F. Chen, and Y. Sun, "FE Reduced-Order Model-Informed Neural Operator for Structural Dynamic Response Prediction," *Neural Networks* 188 (2025): 107437.

52. J. Xie, Y. Xu, Z. Meng, et al., "Bayesian-Driven Modulation of Recoverable Strain in Compliant Auxetic Cementitious Composites for Optimal Energy Harvesters," *Materials & Design* 264 (2026): 115745.

53. S. Fang, J. Liu, Y. Guo, et al., "High-Power-Density Energy Harvester via Optimized Negative Poisson's Ratio Metastructure With Nonlinear Gradient Wall Thickness," *Energy* 354 (2026): 140984.

54. W. Xu, D. Wang, J. Zhang, et al., "Enhanced Energy Absorption in Re-Entrant Honeycombs via Elliptical Double-Arrow Hybrid Design," *Thin-Walled Structures* 230 (2026): 115252.

55. S. Kambampati, H. Chung, and H. A. Kim, "A Discrete Adjoint Based Level Set Topology Optimization Method for Stress Constraints," *Computer Methods in Applied Mechanics and Engineering* 377 (2021): 113563.

56. M. Meßmer, R. N. Asl, S. Kollmannsberger, R. Wüchner, and K.-U. Bletzinger, "Shape Optimization of Embedded Solids Using Implicit Vertex-Morphing," *Computer Methods in Applied Mechanics and Engineering* 426 (2024): 116999.

57. S. Blauth and C. Leithäuser, "Enforcing Mesh Quality Constraints in Shape Optimization With a Gradient Projection Method," *Computer Methods in Applied Mechanics and Engineering* 448 (2026): 118451.

58. Y. Liang, X. Yan, and G. Cheng, "Explicit Control of 2D and 3D Structural Complexity by Discrete Variable Topology Optimization Method," *Computer Methods in Applied Mechanics and Engineering* 389 (2022): 114302.

59. L. Jin, S. Yu, J. Cheng, et al., "Machine Learning Powered Inverse Design for Strain Fields of Hierarchical Architectures," *Composites Part B: Engineering* 299 (2025): 112372.

60. L. Jin, S. Yu, J. Cheng, et al., "Machine Learning-Driven Forward Prediction and Inverse Design for 4D Printed Hierarchical Architecture With Arbitrary Shapes," *Applied Materials Today* 40 (2024): 102373.

61. L. Jin, X. Zhai, J. Jiang, K. Zhang, and W.-H. Liao, "Optimizing Stimuli-Based 4D Printed Structures: A Paradigm Shift in Programmable Material Response," in *Sensors and Smart Structures Technologies for Civil, Mechanical, and Aerospace Systems 2024*, vol. 12949 (SPIE, 2024), 321–332.

62. L. Jin, K. Zhang, S. Zhou, G. Xie, and W.-H. Liao, "Modulus Tunability in Hierarchical Architectures: A Machine Learning-Enabled Approach," in *Multifunctional Materials and Structures 2025*, vol. 13433 (SPIE, 2025), 133–143.

63. R. Agromayor, N. Anand, J.-D. Müller, M. Pini, and L. O. Nord, "A Unified Geometry Parametrization Method for Turbomachinery Blades," *Computer-Aided Design* 133 (2021): 102987.

64. A. Majeed, M. Rafique, J. Y. Abdullah, Z. A. Rajion, et al., "NURBS Curves With the Application of Multiple Bones Fracture Reconstruction," *Applied Mathematics and Computation* 315 (2017): 70–84.

21983844, 0, Downloaded from https://advanced.onlinelibrary.wiley.com/doi/10.1002/advs.78735 by Liuchao Jin , Wiley Online Library on [18/11/2026]. See the Terms and Conditions (https://onlinelibrary.wiley.com/terms-and-conditions) on Wiley Online Library for rules of use; OA articles are governed by the applicable Creative Commons License

65. A. Bauer, M. Breitenberger, B. Philipp, R. Wüchner, and K.-U. Bletzinger, "Embedded Structural Entities in NURBS-Based Isogeometric Analysis," *Computer Methods in Applied Mechanics and Engineering* 325 (2017): 198–218.

66. L. A. Piegl and W. Tiller, "Parametrization for Surface Fitting in Reverse Engineering," *Computer-Aided Design* 33, no. 8 (2001): 593–603.

67. W.-C. Xie, X.-F. Zou, J.-D. Yang, and J.-B. Yang, "Iteration and Optimization Scheme for the Reconstruction of 3D Surfaces Based on Non-Uniform Rational B-Splines," *Computer-Aided Design* 44, no. 11 (2012): 1127–1140.

68. S. Zhou, K. Zhang, L. Jin, Q. Gao, and W.-H. Liao, "Efficient Data Driven Optimization Framework for Designing B-Spline Honeycombs With Excellent Energy Absorption," *Thin-Walled Structures* 209 (2025): 112941.

69. S. Zhou, Q. Gao, L. Jin, G. Xie, K. Zhang, and W.-H. Liao, "Cellular Material Network: A General Machine Learning Architecture for Predicting Mechanical Properties of Cellular Materials," *Advanced Intelligent Systems* (2026): e70501, https://doi.org/10.1002/aisy.70501.

70. W. Lin, L. Jin, Z. Jiang, et al., "Machine Learning-Based Inverse Design for Functional Materials: Methods, Challenges, and Engineering Applications," *Advanced Functional Materials* 36, no. 40 (2026): e75070.

71. L. Zhou, Y. Ohm, R.-M. Chin, O. Kerr, K. Manohar, and M. H. Malakooti, "Machine Learning-Assisted Inverse Design of Soft and Multifunctional Hybrid Liquid Metal Composites," *Advanced Functional Materials* 36 (2026): e75719.

72. K. Wang, X. Lu, T. Liu, et al., "From Artificial to Embodied and Physical Intelligence in Smart Manufacturing," *Advanced Science* 14 (2026): e78384.

73. N. Mortazavi and S. Ziaei-Rad, "Energy Harvesting From Vibrations of a Beam Under Moving Mass Using Auxetic Cantilever Beams: Theoretical and Experimental Investigations," *Mechanics of Advanced Materials and Structures* 32, no. 5 (2025): 991–1027.

74. L. Wang, L. Zhao, Z. Jiang, et al., "Contribution Discrimination of Auxetic Cantilever for Increased Piezoelectric Output in Vibration Energy Harvesting," in *2021 IEEE 16th International Conference on Nano/Micro Engineered and Molecular Systems (NEMS)* (IEEE, 2021), 513–517.

75. A. K. Tikariha, N. Saurabh, V. Gudipadu, and S. Patel, "Effect of Auxetic Structures Parameters Variation on PVDF-Based Piezoelectric Energy Harvesters," *Journal of Applied Physics* 132, no. 24 (2022): 244105.

76. H. Zhang, S. Chen, M. Karimi, B. Li, S. Saydam, and M. Hassan, "Numerical and Experimental Investigation of an Auxetic Piezoelectric Energy Harvester With Frequency Self-Tuning Capability," *Smart Materials and Structures* 33, no. 5 (2024): 055022.

Supporting Information

Additional supporting information can be found online in the Supporting Information section.

Supporting File 1: advs78735-sup-0001-SuppMat.pdf.

Supporting File 2: advs78735-sup-0002-VideoS1.mp4.

21983844, 0, Downloaded from https://advanced.onlinelibrary.wiley.com/doi/10.1002/advs.78735 by Liuchao Jin , Wiley Online Library on [18/11/2026]. See the Terms and Conditions (https://onlinelibrary.wiley.com/terms-and-conditions) on Wiley Online Library for rules of use; OA articles are governed by the applicable Creative Commons License